NASA/CR-1998-206943

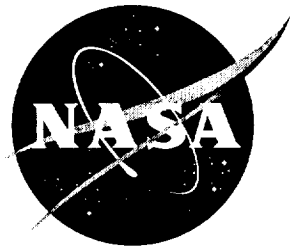

Euler Technology Assessment - SPLITFLOW Code Applications for Stability and Control Analysis on an Advanced Fighter Model Employing Innovative Control Concepts

Keith J. Jordan
Lockheed Martin Tactical Aircraft Systems, Fort Worth, Texas

National Aeronautics and
Space Administration

Langley Research Center
Hampton, Virginia 23681-2199

Prepared for Langley Research Center
under Contract NAS1-96014

March 1998

Available from the following:

NASA Center for AeroSpace Information (CASI)
800 Elkridge Landing Road
Linthicum Heights, MD 21090-2934
(301) 621-0390

National Technical Information Service (NTIS)
5285 Port Royal Road
Springfield, VA 22161-2171
(703) 487-4650

Table of Contents

List of Figures

List of Tables

Euler Technology Assessment- SPLITFLOW Code Applications for Stability and Control Analysis on an Advanced Fighter Model Employing Innovative Control Concepts

Keith Jordan
Lockheed Martin Tactical Aircraft Systems
Fort Worth, Texas

Summary

This report documents results from the NASA/Langley sponsored Euler Technology Assessment Study conducted by Lockheed Martin Tactical Aircraft Systems (LMTAS). The purpose of the study was to evaluate the ability of the SPLITFLOW code using viscous and inviscid flow models to predict aerodynamic stability and control of an advanced fighter model. The inviscid flow model was found to perform well at incidence angles below approximately 15 deg, but not as well at higher angles of attack. The results using a turbulent, viscous flow model matched the trends of the wind tunnel data, but did not show significant improvement over the Euler solutions. Overall, the predictions were found to be useful for stability and control design purposes.

Nomenclature

C_p Pressure Coefficient, $C_p = (P - P_\infty)/Q_\infty$

C_A Axial Force Coefficient, C_A = (Force in $-X_B$ direction)/($Q_\infty S$).

C_Y Lateral Force Coefficient, C_Y= (Force in Y_B direction)/($Q_\infty S$).

C_N Normal Force Coefficient, C_N = (Force in $-Z_B$ direction)/($Q_\infty S$).

C_l Rolling Moment Coefficient, C_l = (Moment about the X_B axis)/($Q_\infty SL$).

C_m Pitching Moment Coefficient, C_m = (Moment about the Y_B axis)/($Q_\infty SL$).

C_n Yawing Moment Coefficient, C_n = (Moment about the Z_B axis)/($Q_\infty SL$).

L Reference Length (1.5972 ft, Model Scale)

M Free-stream Mach number

P Pressure

P_∞ Free-stream Pressure

Q_∞ Dynamic Pressure, $Q_\infty = \frac{1}{2} \rho_\infty V_\infty^2$

S Reference Area (2.4957 ft^2, Model Scale)

V_∞ Free-stream Velocity

X_B Reference axis parallel to the intersection of the waterline 0.0 reference plane and the aircraft symmetry plane, originating at the aircraft center of rotation. The positive direction is from the tail toward the nose of the aircraft.

Y_B Reference axis perpendicular to the X_B axis, parallel to the waterline 0.0 plane. The positive direction is toward the right wing tip of the aircraft from the pilot's point of view.

Z_B Reference axis perpendicular to the X_B and Y_B axis lying parallel to the symmetry plane of the aircraft. The positive direction is downward from the pilot's point of view.

α Angle of Attack

β Angle of Sideslip

ρ_∞ Free-stream Density

σC_A Standard deviation of the averaged C_A values.

σC_Y Standard deviation of the averaged C_Y values.

σC_N Standard deviation of the averaged C_N values.

σC_l Standard deviation of the averaged C_l values.

σC_m Standard deviation of the averaged C_m values.

σC_n Standard deviation of the averaged C_n values.

1.0 Introduction

The purpose of this study was to evaluate the ability of the SPLITFLOW code to predict aerodynamic stability and control of an advanced fighter configuration. Currently at LMTAS, designers are limited in predictive capability to linear or empirical methods. Therefore, a method which can predict non-linear effects on new geometries is a very attractive proposition. To assess the applicability of the SPLITFLOW code to stability

and control studies, solutions were obtained which predict compressibility effects, viscous effects at a range of α, control deflection effects at a range of α, and lateral/directional stability for a range of β. The effect of two different trailing edge geometries was also investigated. Convergence characteristics and correlation of the CFD predictions with wind tunnel data are provided.

The SPLITFLOW code is an upwind, unstructured, finite-volume Euler/Navier-Stokes code. It utilizes a Cartesian mesh topology in inviscid regions and a prismatic mesh with a k-kl turbulence model in viscous regions. The code automatically generates the volume mesh, after a suitable surface description has been supplied, and includes automatic refinement/de-refinement of the initial cartesian volume mesh as the solution progresses. Further details of mesh generation and the numerical formulation are included in Ref. 1.

2.0 Methodology

The LMTAS designed generic high-sweep delta wing model, developed under the DoD sponsored Innovative Control Effectors (ICE) program, was chosen as the subject geometry (see Fig. 1), and will henceforth be referred to as the ICE model. The configurations of interest were $1/18^{th}$ scale wind tunnel models with a 65 deg leading edge sweep, deployable spoilers and elevons, and a straight or serrated trailing edge. The serrated trailing edge configuration with no deflected control surfaces is the baseline configuration. The planned computational matrix for the study is presented in Table 1.

Two issues were encountered with the model geometry at the beginning of the project. The first involved the CAD description of the ICE model. Usually, the mesh boundaries for SPLITFLOW are created using internal functions of the LMTAS developed CAD package called ACAD. However, for this geometry, the CAD description has many gaps and overlapping surfaces that exceed the tolerances required by ACAD to construct a mesh (see Fig. 2). The ACAD description could not be fixed in a reasonable amount of time because the analytical descriptions needed to define the surfaces within the tolerances no longer exist in an ACAD format. The solution was to use a structured surface mesh to construct the tetrahedral surface mesh required in SPLITFLOW. The structured grid generator used at LMTAS, GRIDGEN, is better able to span the gaps and overlaps in the CAD geometry. Once constructed, the cells of the structured surface mesh were divided into triangles and used by SPLITFLOW. The resulting surfaces are shown in Figs. 3a-d. This was the first application of this methodology to a real geometry, and could be useful in the future if similar problems are encountered. Later in the study, for the deflected control cases, a method to combine the meshing capabilities of ACAD and GRIDGEN was developed, further enhancing the surface mesh generation capability. It should be noted that one of the great strengths of the SPLITFLOW code is the ability to incorporate an unstructured surface mesh automatically generated by ACAD directly into the flow solver without the time-consuming construction of a computational surface and flowfield mesh by hand. While the construction of the structured surface mesh is more time consuming than the automatic surface mesh construction implemented

in ACAD, the effort exerted to obtain the surface mesh is still small compared to that required for a full structured volume mesh. Additionally, for some configurations, it is possible that starting from a structured mesh could result in a superior unstructured mesh because the structured mesh generator will allow more control over the surface point distribution than will ACAD.

The second issue involved the thin, sharp trailing edge of the wing and the oct-tree mesh refinement methodology used in SPLITFLOW. With oct-tree refinement, if a cell is split, it will be split into eight equal-sized cells, and no cell can have an edge that is less than half as long as an adjacent edge. Therefore, sharp convex regions cause recursive refinement of the grid and may result in an unacceptably large number of cells. A 2-D representative sketch of the effect is presented in Fig. 4. If such a situation occurs, memory requirements are increased and the maximum CFL number that can be used is decreased. In the past, the problem had been handled by removing a small part of the trailing edge of the wing so that the resulting thickness at the trailing edge was approximately $1/8^{th}$ inch full scale (see Fig. 4b). The $1/8^{th}$ inch thickness was chosen because the measured trailing edge thickness of the wing of an F-16 is $1/8^{th}$ inch, and is assumed to be typical. However, removing part of the wing of the ICE model was not a viable option because the wing is so thin that an unacceptable amount of the wing planform would be removed to obtain the desired thickness. A solution to avoid the difficulty was to create a prismatic mesh around the body. When using a prismatic mesh, the SPLITFLOW code refines the cartesian volume mesh around the larger and thicker boundary created by the outer prismatic layer, thus eliminating the problem with the thin wing. Even though prismatic meshes are typically used in viscous flow solutions to adequately resolve the boundary layer regions, a prismatic mesh can be used in an inviscid flow solution if a larger normal spacing and an inviscid boundary condition are used. Another option that was investigated was a version of the code that implemented an omni-tree refinement algorithm to create the cartesian mesh. The omni-tree refinement algorithm allows high aspect ratio cells to be generated, thus reducing the number of cells required to define the trailing edge (see Fig. 4c), and eliminating the need for the prismatic mesh in the inviscid calculations. The omni-tree refinement method was used to obtain the varying β solutions and the $M = 0.9$, $\alpha = 18$, 20, and 25 deg solutions for the baseline case, and the standard oct-tree refinement method was used to obtain the remaining solutions.

3.0 Solutions from Computational Matrix

Computer Requirements

Convergence was determined by the trends of the force and moment predictions, not the residuals. Because of the effect of grid refinement and flux limiters on the residuals, load coefficients were thought to be a better measure of convergence. For the inviscid solutions, the number of solver iterations required was a function of α. Usually, for α under 20 deg, the solver required 1000-3000 steps to converge with a maximum CFL varying from 1.0 to 3.0. These values for CFL are lower than are usually possible and are

thought to be caused by the small cells in the prismatic mesh. For $\alpha \geq 20$ deg, the number of iterations ranged between 2000-6000 and rarely allowed a CFL of over 1.0. For the viscous solutions, 4000- 5000 iterations were required and a CFL of 0.5 or 1.0 was used. For about half of the solutions, the loads converged smoothly to an answer (see Fig. 5a). However, in the other half of the cases, the load predictions oscillated about some mean and never became completely smooth (see Fig. 5b). The final load predictions were obtained by averaging the tabulated loads near the end of the runs. The load predictions from the last 100 iterations were averaged for the smoothly converging cases, and from the last 500 iterations for the oscillating cases. The load predictions and wind tunnel data are presented in Table 2. As an indication of the variation in the load predictions, the standard deviations of the averages were calculated and are presented in Table 3.

During the solution process, the inviscid calculations typically required approximately 0.3×10^{-3} cpusec/step/cell, and the viscous calculations required approximately 0.5×10^{-3} cpusec/step/cell on a Cray J-90 computer. Note that because the number of cells changes over the course of a solution, these numbers can only give a rough idea of the total CPU time that is required. In this study, the CPU time required to obtain the inviscid solutions ranged from 50 to 200 cpuhrs, and the CPU time required to obtain the viscous solutions ranged from 400 to 600 cpuhrs. Using inputs to the code, the inviscid cartesian meshes were limited to 300,000 cells, the viscous cartesian meshes were limited to 400,000 cells, and the cartesian mesh used with the omni-tree refinement method was limited to 800,000 cells. The number of cells in the prismatic layers varied with the configuration, and were not used at all for the β cases. The baseline prismatic mesh contained approximately 268,000 cells, the deflected elevon prismatic mesh contained approximately 278,000 cells, the deflected spoiler prismatic mesh contained approximately 526,000 cells, the straight trailing edge prismatic mesh contained approximately 261,000 cells, and the viscous baseline prismatic mesh contained approximately 783,000 cells.

Compressibility Effects

Solutions for the baseline case at M = 0.6, 0.9, and 1.2 were obtained to assess the ability of SPLITFLOW to predict compressibility effects. Contour plots of the resulting surface C_p distributions at α= 10 and 20 deg for each Mach number are presented in Fig. 6. The C_p distributions shown are consistent with expectations, characterized by a vortex and the associated pressure drop near the leading edge, a pressure drop behind the maximum cross-sectional area of the canopy, and a pressure rise near the rear of the canopy. The M= 0.9, α = 10 deg case also has a normal shock wave near the tail of the aircraft that is not present in any of the other solutions. Particle traces for the α = 10 and 20 deg, M = 0.6, 0.9, and 1.2 solutions are included in Fig. 7. The CFD load predictions are plotted with the corresponding wind tunnel data in Fig. 8. Also included in Fig. 8 are C_A predictions corrected with a viscous drag increment which were obtained with empirical methods available at LMTAS. In all cases, the predictions match the wind tunnel data fairly well. In none of the cases does the addition of the viscous drag increment

significantly improve the agreement of the CFD predictions and the wind tunnel data. For completeness, a tabulation of the CFD predictions (which do not include the viscous corrections for C_A) and the wind tunnel data is included in Table 2.

Viscous Effects

To assess the ability of SPLITFLOW to predict viscous effects, inviscid and viscous solutions were obtained on the baseline case at M = 0.9, α = 10, 15, 18, 20, and 25 deg. Solutions for the deflected spoiler cases were planned but were not obtained because of stability problems and time constraints. Contour plots of C_p for α= 10 and 20 deg for each Mach number appear in Fig. 9. As for the inviscid cases, each solution predicts a vortex trailing from the leading edge at some point. Comparing the C_p distributions on the upper surface in Fig. 9a to the upper surface distributions in Fig. 6c, it can be seen that, for the α = 10 deg condition, the pressure drop caused by the vortex on the viscous solution is not as large as that predicted by the inviscid solution, and the shocks are more smeared in the viscous solution, as would be expected. However, the shock near the tail in the inviscid solution does not appear in the viscous solution. Close inspection of the solution show that the Mach number increase over the leading edge is lower in the viscous solution than that of the inviscid solution, resulting in the loss of the shock wave. The C_p distributions at α = 20 deg are very similar, but with the viscous case having the pressure gradients more smeared. Figure 10 shows particle traces for the viscous and inviscid solutions at α = 10 and 20 deg. The specified starting locations for the particle traces are not fine enough to locate it, but a very small vortex is present near the wing leading edge in the α = 10 deg case. Contour plots of normalized stagnation pressure 2.0 ft downstream of the nose are presented in Fig. 11. In Figs. 10 and 11, it can be seen that the vortex in the α = 10 deg viscous solution is slightly larger, and more inboard from the leading edge than for the inviscid solution. Further examination of the solutions also show that the maximum Mach number in the vortex of the inviscid solution is generally higher than that in the viscous solution. This behavior is consistent with viscous versus inviscid flow predictions. For the α = 20 deg condition, the maximum Mach number in the vortex of the inviscid solution is higher than that in the viscous solution, as expected. However, the vortex predicted by the viscous calculations is less inboard and is smaller than that predicted with the inviscid solution (see Figs. 10 and 11). The cause for the discrepancy in size and location is unclear. Possible causes include differences in the grid when using the omni-tree refinement for the inviscid case from the oct-tree refinement and prismatic mesh used in the viscous case (differences in refinement are apparent from the shading patterns in Fig. 11 c and d), and differences in the flow solvers. The omni-tree SPLITFLOW uses an extrapolation scheme that extrapolates in the normal direction only and can be no higher than second order, while the oct-tree SPLITFLOW extrapolation scheme includes cross terms and can be up to a third order scheme. The inviscid and viscous load predictions are presented in Fig. 12, and the predictions are compared to wind tunnel data in Table 2. With the inclusion of the viscous effects for the baseline model, the CFD predictions for the lift and pitching moment are not significantly improved, and, surprisingly, the prediction for C_A does not agree as well. Prior experience with SPLITFLOW has shown that a finely resolved leading edge is critical in

obtaining good total drag predictions. It is possible that the surface mesh at the leading edge was not refined well enough. The exact degree of refinement necessary is not currently known.

Control Effects

To assess the ability of SPLITFLOW to predict the effects of deflected control surfaces using an inviscid flow model, solutions for two different ICE configurations were obtained. Both incorporated the serrated trailing edge, but one configuration modeled a symmetric 30 deg deflection of the elevons, while the other modeled the non-symmetric 60 deg deflection of the spoiler. Inviscid flow field solutions were obtained at M = 0.9, α= 8, 10, 12, 14, 16, 18, 20, and 22 deg for both configurations. The resulting surface C_p distributions for α = 10 and 20 deg are included in Fig. 13. Particle trace plots are included in Fig. 14. As can be seen from the figures, the deflected surfaces significantly change the nature of the flow. The deflected elevons eliminate the vortices at α = 10 deg. The deflected spoiler eliminates the starboard vortex at both angles of attack, and greatly reduces the size of the port vortex at α = 10 deg. The load predictions are plotted with the corresponding wind tunnel data in Fig. 15 . For both configurations, the trends generally agree with the wind tunnel data, with the disagreement increasing with the larger angles of attack. As the angle of attack increases, the inviscid flow model is less able to accurately capture the physics of the flow. Increments from the baseline case are included in Fig. 16. The agreement for the predicted increments with wind tunnel data is acceptable for the spoiler case, but less so for the elevon case.

Lateral Direction

To assess the ability of SPLITFLOW to predict the effects of a yawed model, inviscid solutions were obtained on the serrated trailing edge model at M = 0.9, α = 20, β = 1, 2, 3, 4, 5, and 8 deg. As noted earlier, an experimental version of SPLITFLOW that implements omni-tree refinement to construct the cartesian mesh was used for these calculations, and the prismatic mesh was not required. The resulting C_p distributions for β = 4 and 8 deg are shown in Fig. 17. Particle traces are plotted in Fig. 18. To better show the asymmetry of the vortices, contour plots of normalized stagnation pressure at 2.0 ft downstream of the nose are included in Fig. 19. The force and moment coefficients are plotted with the corresponding wind tunnel data in Fig. 20, and a tabulation of the predictions and the wind tunnel data is included in Table 2. The agreement of the results are mixed. Predictions for the forces are acceptable, but the agreement for the moment predictions are less so. Once again, the inviscid flow model is inadequate for modeling the viscous effects at the larger total incidence angles.

Effect of Trailing Edge Geometry

To determine the effect of the wing trailing edge geometry, solutions for the serrated and straight trailing edge model were obtained at M = 0.9 at 10, 15, 20, and 25 deg angle of attack. Surface C_p distributions for α = 10 and 20 appear in Fig. 21. The distributions are very similar to the baseline serrated-edge case. The most obvious difference being in the shape of the shock near the tail. Particle traces for α= 10 and 20 deg appear in Fig. 22.

with no vortex over the wing, but more disordered at α= 20 deg. A comparison of normalized stagnation pressure for the baseline and straight trailing edge cases at 2.0 ft from the nose are included in Fig. 23. Even with the differences in the flow pattern, the vortex size and pressures are very similar. The CFD load predictions are compared to the wind tunnel data in Fig. 24. In general, the results are acceptable, predicting the nonlinearity in the curves. A tabulation of the CFD predictions and the wind tunnel data is included in Table 2.

4.0 Conclusions

From a stability and control standpoint, SPLITFLOW is a valuable addition to tools already in use at LMTAS. It has demonstrated an ability to predict trends in loads, with some problems occurring with the inviscid solutions at larger angles of attack, as would be expected. The immaturity of the viscous capability in the SPLITFLOW code was demonstrated by the inaccuracies in the viscous solutions. Development of the viscous capability is continuing and improved predictions are expected in the near future. Several new methods of grid construction were investigated. To obtain solutions for geometries for which a surface mesh are not easily obtained, three methods for grid construction were investigated. The omni-tree refinement method, a method using a structured surface mesh to construct the SPLITFLOW facets, and a method combining ACAD unstructured meshes and GRIDGEN structured meshes were found to be viable options in dealing with difficult geometries.

Additional analysis that would be recommended include further investigation into the ability of SPLITFLOW to predict the changes in the slope of the C_m curves. Further investigations into other types of controls could be conducted as well, including moving wing tips and slotted spoilers.

5.0 Acknowledgments

This effort was sponsored by NASA-Langley Research Center under Contract NAS-1-96014. Significant technical guidance was provided by Farhad Ghaffari of the Transonic/Supersonic Aerodynamics Branch of NASA-Langley Research Center. His assistance is gratefully acknowledged. Computer time on the C-90 machine 'vonneumann' of the National Aerodynamic Simulator was provided by NASA-Ames Research Center.

References

1. Karman, S.L., Jr. "SPLITFLOW: A 3D Unstructured Cartesian/Prismatic Grid CFD Code for Complex Geometries", AIAA-95-0343, January 1995.

Table 1. Computational Matrix

Configuration	Mach	α	β	Flow Model	Final Status
Baseline	0.6	10	0	Euler	complete
		15	0	Euler	complete
		20	0	Euler	complete
	0.9	10	0	Euler	complete
		15	0	Euler	complete
		18	0	Euler	complete
		20	0	Euler	complete
		25	0	Euler	complete
	1.2	10	0	Euler	complete
		15	0	Euler	complete
		20	0	Euler	complete
	0.9	20	1	Euler	complete
		20	2	Euler	complete
		20	3	Euler	complete
		20	4	Euler	complete
		20	5	Euler	complete
		20	8	Euler	complete
Baseline w/ Deflected Spoiler	0.9	8	0	Euler	complete
		10	0	Euler	complete
		12	0	Euler	complete
		14	0	Euler	complete
		15	0	Euler	complete
		16	0	Euler	complete
		18	0	Euler	complete
		20	0	Euler	complete
		22	0	Euler	complete
		25	0	Euler	complete
Baseline w/Deflected Elevon	0.9	8	0	Euler	complete
		10	0	Euler	complete
		12	0	Euler	complete
		14	0	Euler	complete
		16	0	Euler	complete
		18	0	Euler	complete
		20	0	Euler	complete
		22	0	Euler	complete
Straight Trailing Edge	0.9	10	0	Euler	complete
		15	0	Euler	complete
		20	0	Euler	complete
		25	0	Euler	complete
Baseline	0.9	10	0	N-S	complete
		15	0	N-S	complete
		18	0	N-S	complete
		20	0	N-S	complete
		25	0	N-S	complete
Baseline w/Deflected Spoiler	0.9	10	0	N-S	incomplete
		15	0	N-S	incomplete
		18	0	N-S	incomplete
		20	0	N-S	incomplete
		25	0	N-S	incomplete

Table 2. Force and Moment Comparisons, Body Axis System

Config	M	α	β	C_A	C_A data	C_Y	C_Y data	C_N	C_N data	C_l	C_l data	C_m	C_m data	C_n	C_n data	Model
baseline	0.6	10	0	-0.0251	-0.0209	-	-	0.3662	0.3585	-	-	-0.0081	-0.0029	-	-	Euler
		15	0	-0.0327	-0.0285	-	-	0.6313	0.6572	-	-	-0.0147	-0.0110	-	-	Euler
		20	0	-0.0391	-0.0420	-	-	0.8775	0.9388	-	-	-0.0121	-0.0102	-	-	Euler
	0.9	10	0	-0.0222	-0.0196	-	-	0.4283	0.4040	-	-	-0.0207	-0.0099	-	-	Euler
		15	0	-0.0270	-0.0215	-	-	0.7120	0.6933	-	-	-0.0395	-0.0290	-	-	Euler
		18	0	-0.0147	-0.0173	-	-	0.7336	0.7707	-	-	-0.0212	-0.0144	-	-	Euler
		20	0	-0.0105	-0.0174	-	-	0.7794	0.8490	-	-	-0.0258	-0.0172	-	-	Euler
		25	0	-0.0056	-0.0184	-	-	0.8900	1.0299	-	-	-0.0403	-0.0303	-	-	Euler
	1.2	10	0	0.0006	0.0039	-	-	0.4405	0.4343	-	-	-0.0517	-0.0468	-	-	Euler
		15	0	-0.0075	-0.0030	-	-	0.6871	0.6703	-	-	-0.0832	-0.0736	-	-	Euler
		20	0	-0.0079	-0.0062	-	-	0.9109	0.8809	-	-	-0.1038	-0.0888	-	-	Euler
	0.9	20	1	-0.0099	-0.0223	-0.0039	-0.0038	0.7697	0.8382	0.0035	-0.0012	-0.0280	-0.0175	-0.0005	0.0002	Euler
		20	2	-0.0078	-0.0224	-0.0037	-0.0043	0.7731	0.8369	-0.0021	-0.0030	-0.0315	-0.0171	-0.0017	0.0004	Euler
		20	3	-0.0064	-0.0249	-0.0089	-0.0099	0.7660	0.8594	0.0036	0.0041	-0.0361	-0.0195	-0.0022	-0.0015	Euler
		20	4	-0.0093	-0.0250	-0.0075	-0.0120	0.7801	0.8625	-0.0028	0.0038	-0.0314	-0.0220	-0.0035	-0.0014	Euler
		20	5	-0.0104	-0.0241	-0.0134	-0.0141	0.7725	0.8642	0.0053	0.0043	-0.0285	-0.0253	-0.0033	-0.0017	Euler
		20	8	-0.0109	-0.0226	-0.0176	-0.0168	0.7889	0.8444	0.0031	0.0024	-0.0329	-0.0257	-0.0055	-0.0018	Euler
straight t.e.	0.9	10	0	-0.0172	-0.0137	-	-	0.4175	0.4325	-	-	-0.0111	-0.0075	-	-	Euler
		15	0	-0.0258	-0.0251	-	-	0.6687	0.6545	-	-	-0.0214	-0.0184	-	-	Euler
		20	0	-0.0147	-0.0222	-	-	0.7534	0.8425	-	-	-0.0124	-0.0168	-	-	Euler
		25	0	-0.0122	-0.0254	-	-	0.8710	1.0369	-	-	-0.0263	-0.0293	-	-	Euler
baseline	0.9	8	0	0.0438	0.0379	-0.0256	-0.0300	0.2333	0.1545	0.0191	0.0220	0.0034	0.0234	0.0204	0.0140	Euler
+ spoiler		10	0	0.0339	0.0260	-0.0276	-0.0294	0.3242	0.2423	0.0193	0.0242	-0.0007	0.0205	0.0203	0.0120	Euler
		12	0	0.0225	0.0148	-0.0285	-0.0276	0.4086	0.3715	0.0240	0.0232	-0.0043	0.0095	0.0186	0.0082	Euler
		14	0	0.0158	0.0051	-0.0209	-0.0213	0.5271	0.5100	0.0271	0.0242	-0.0136	-0.0045	0.0135	0.0034	Euler
		15	0	0.0133	0.0096	-0.0211	-0.0183	0.5839	0.6284	0.0171	0.0224	-0.0164	-0.0088	0.0143	0.0014	Euler
		16	0	0.0084	-0.0014	-0.0175	-0.0183	0.6439	0.6285	0.0269	0.0224	-0.0214	-0.0088	0.0110	0.0014	Euler
		18	0	0.0013	-0.0040	-0.0141	-0.0130	0.7408	0.7213	0.0157	0.0148	-0.0254	-0.0128	0.0087	0.0011	Euler
		20	0	-0.0047	-0.0102	-0.0063	-0.0094	0.8184	0.8078	0.0058	0.0100	-0.0220	-0.0111	0.0049	0.0011	Euler
		22	0	0.0008	-0.0147	0.0063	-0.0061	0.8479	0.8962	-0.0128	0.0073	-0.0317	-0.0145	0.0042	0.0003	Euler
		25	0	-0.0025	-0.0215	0.0172	-0.0038	0.9425	1.0195	-0.0222	0.0059	-0.0407	-0.0247	0.0031	-0.0006	Euler

Table 2. Concluded

Config	M	α	β	C_A	C_A data	C_Y	C_Y data	C_N	C_N data	C_l	C_l data	C_m	C_m data	C_n	C_n data	Model
baseline	0.9	8	0	0.0170	0.0088	-	-	0.4725	0.4692	-	-	-0.0758	-0.0735	-	-	Euler
+ elevon		10	0	0.0009	0.0051			0.5571	0.5722			-0.0740	-0.0812			
		12	0	0.0020	0.0069	-	-	0.6601	0.6985	-	-	-0.0825	-0.0935	-	-	Euler
		14	0	0.0000	0.0087	-	-	0.7847	0.8196	-	-	-0.0941	-0.1019	-	-	Euler
		16	0	-0.0004	0.0084	-	-	0.8728	0.9151	-	-	-0.0949	-0.1045	-	-	Euler
		18	0	-0.0016	0.0091	-	-	0.9707	0.9580	-	-	-0.0995	-0.0880	-	-	Euler
		20	0	0.0100	0.0099	-	-	0.8931	0.9709	-	-	-0.0604	-0.0626	-	-	Euler
		22	0	0.0117	0.0094	-	-	0.8435	1.0362	-	-	-0.0502	-0.0632	-	-	Euler
baseline	0.9	10	0	-0.0011	-0.0196	-	-	0.3976	0.4040	-	-	-0.0084	-0.0099	-	-	N-S
		15	0	-0.0101	-0.0215	-	-	0.6251	0.6933	-	-	-0.0155	-0.0290	-	-	N-S
		18	0	-0.0106	-0.0173	-	-	0.7558	0.7707	-	-	-0.0152	-0.0144	-	-	N-S
		20	0	-0.0107	-0.0174	-	-	0.8396	0.8490	-	-	-0.0167	-0.0172	-	-	N-S
		25	0	-0.0119	-0.0184	-	-	1.0204	1.0299	-	-	-0.0229	-0.0303	-	-	N-S

Table 3. Standard Deviation of Averaged Loads

Config.	M	α	β	Model	σC_A	σC_Y	σC_N	σC_l	σC_m	σC_n	Iterations averaged
Baseline	0.6	10	0	Euler	0.0001	-	0.0014	-	0.0008	-	500
		15	0	Euler	0.0005	-	0.0062	-	0.0027	-	500
		20	0	Euler	0.0005	-	0.0105	-	0.0049	-	500
	0.9	10	0	Euler	0.0000	-	0.0000	-	0.0000	-	100
		15	0	Euler	0.0001	-	0.0001	-	0.0001	-	100
		18	0	Euler	0.0000	-	0.0000	-	0.0000	-	100
		20	0	Euler	0.0002	-	0.0021	-	0.0008	-	500
		25	0	Euler	0.0004	-	0.0046	-	0.0017	-	500
	1.2	10	0	Euler	0.0000	-	0.0000	-	0.0000	-	100
		15	0	Euler	0.0000	-	0.0000	-	0.0000	-	100
		20	0	Euler	0.0000	-	0.0000	-	0.0000	-	100
	0.9	20	1	Euler	0.0000	0.0001	0.0014	0.0004	0.0005	0.0000	500
		20	2	Euler	0.0001	0.0002	0.0011	0.0005	0.0006	0.0001	500
		20	3	Euler	0.0003	0.0089	0.0039	0.0022	0.0018	0.0003	500
		20	4	Euler	0.0002	0.0002	0.0018	0.0003	0.0009	0.0001	500
		20	5	Euler	0.0003	0.0002	0.0016	0.0006	0.0009	0.0001	500
		20	8	Euler	0.0003	0.0005	0.0056	0.0013	0.0023	0.0003	500
Straight t.e.	0.9	10	0	Euler	0.0000	-	0.0000	-	0.0000	-	100
		15	0	Euler	0.0000	-	0.0001	-	0.0000	-	100
		20	0	Euler	0.0001	-	0.0001	-	0.0001	-	100
		25	0	Euler	0.0001	-	0.0019	-	0.0009	-	500
Spoiler	0.9	8	0	Euler	0.0001	0.0000	0.0004	0.0000	0.0001	0.0000	100
		10	0	Euler	0.0000	0.0000	0.0001	0.0000	0.0000	0.0000	100
		12	0	Euler	0.0000	0.0002	0.0002	0.0001	0.0001	0.0001	100
		14	0	Euler	0.0000	0.0001	0.0002	0.0000	0.0001	0.0000	100
		15	0	Euler	0.0000	0.0001	0.0001	0.0000	0.0000	0.0001	100
		16	0	Euler	0.0000	0.0001	0.0003	0.0000	0.0000	0.0000	100
		18	0	Euler	0.0000	0.0001	0.0002	0.0000	0.0001	0.0000	100
		20	0	Euler	0.0002	0.0000	0.0007	0.0001	0.0000	0.0000	100
		22	0	Euler	0.0000	0.0000	0.0000	0.0002	0.0001	0.0000	100
		25	0	Euler	0.0001	0.0003	0.0013	0.0005	0.0006	0.0001	500
Elevon	0.9	8	0	Euler	0.0000	-	0.0000	-	0.0000	-	100
		10	0	Euler	0.0000	-	0.0001	-	0.0000	-	100
		12	0	Euler	0.0000	-	0.0000	-	0.0000	-	100
		14	0	Euler	0.0000	-	0.0000	-	0.0000	-	100
		16	0	Euler	0.0000	-	0.0000	-	0.0000	-	100
		18	0	Euler	0.0000	-	0.0000	-	0.0000	-	100
		20	0	Euler	0.0005	-	0.0008	-	0.0007	-	500
		22	0	Euler	0.0004	-	0.0020	-	0.0011	-	500
Baseline	0.9	10	0	N-S	0.0000	-	0.0000	-	0.0000	-	100
		15	0	N-S	0.0000	-	0.0000	-	0.0000	-	100
		18	0	N-S	0.0000	-	0.0001	-	0.0000	-	100
		20	0	N-S	0.0001	-	0.0001	-	0.0001	-	100
		25	0	N-S	0.0000	-	0.0004	-	0.0001	-	100

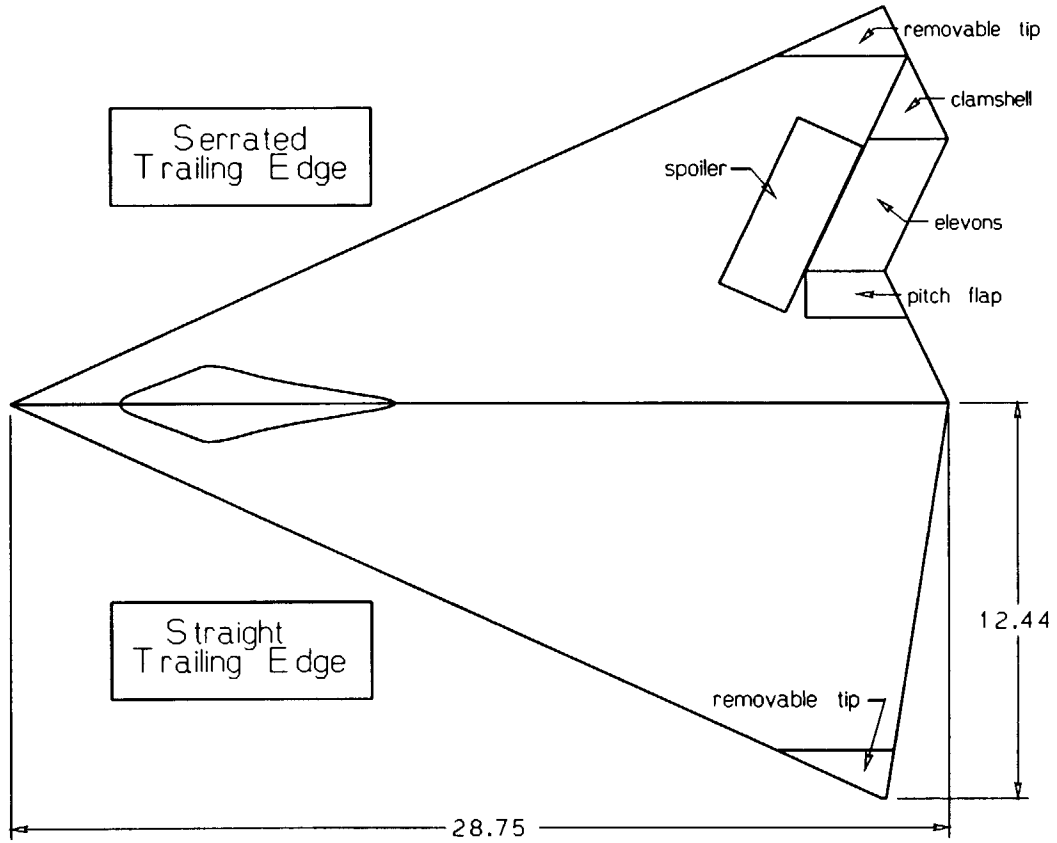

Figure 1. ICE Model Geometry

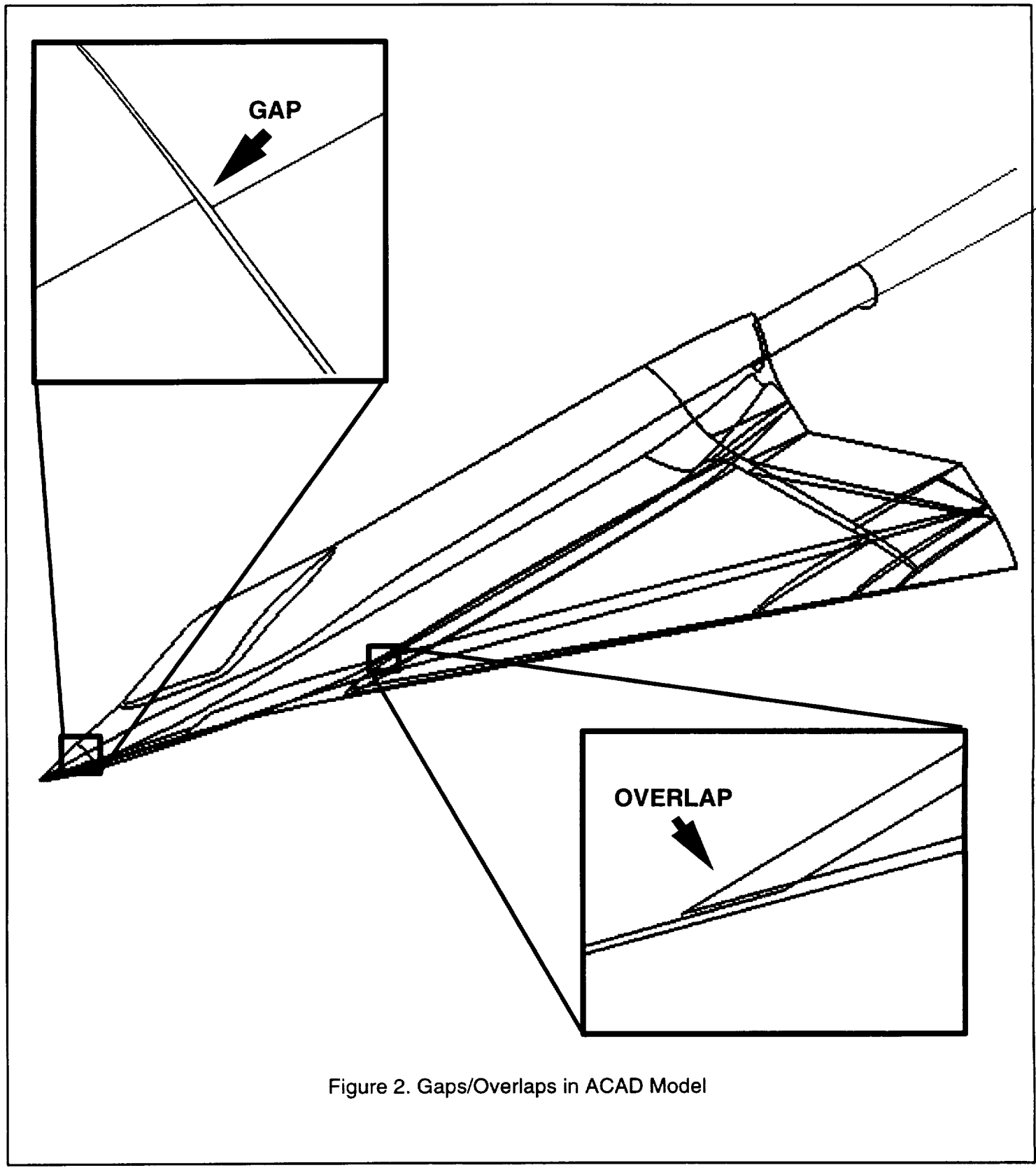

Figure 2. Gaps/Overlaps in ACAD Model

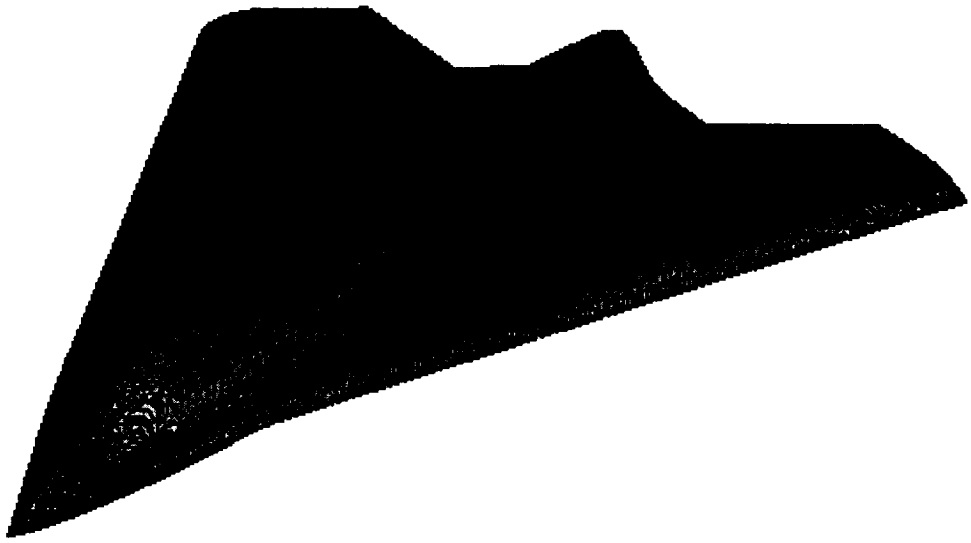

a. Baseline

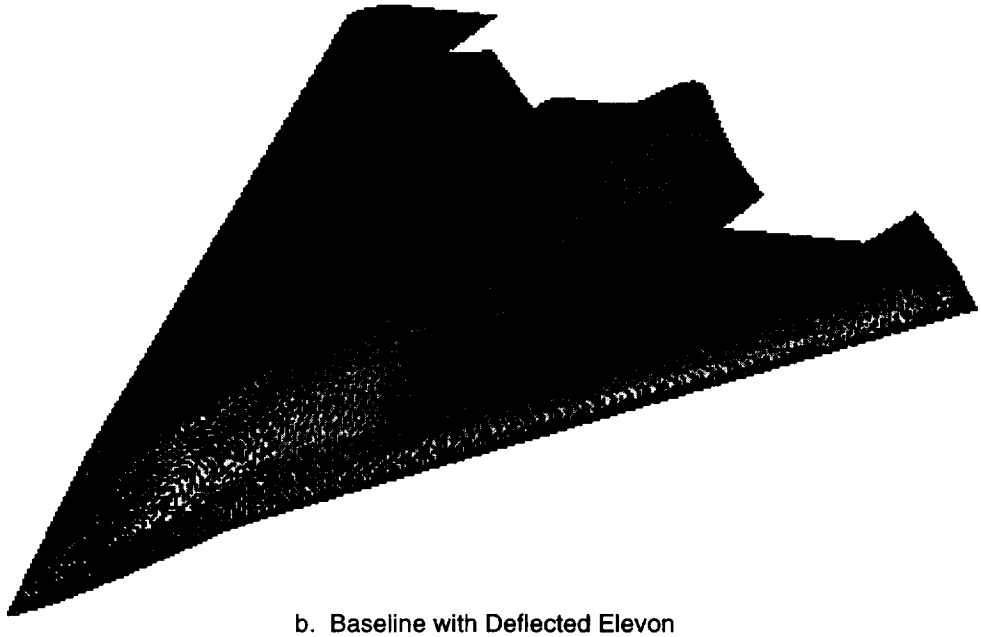

b. Baseline with Deflected Elevon

Figure 3. Configuration Surfaces

c. Baseline with Deflected Spoiler

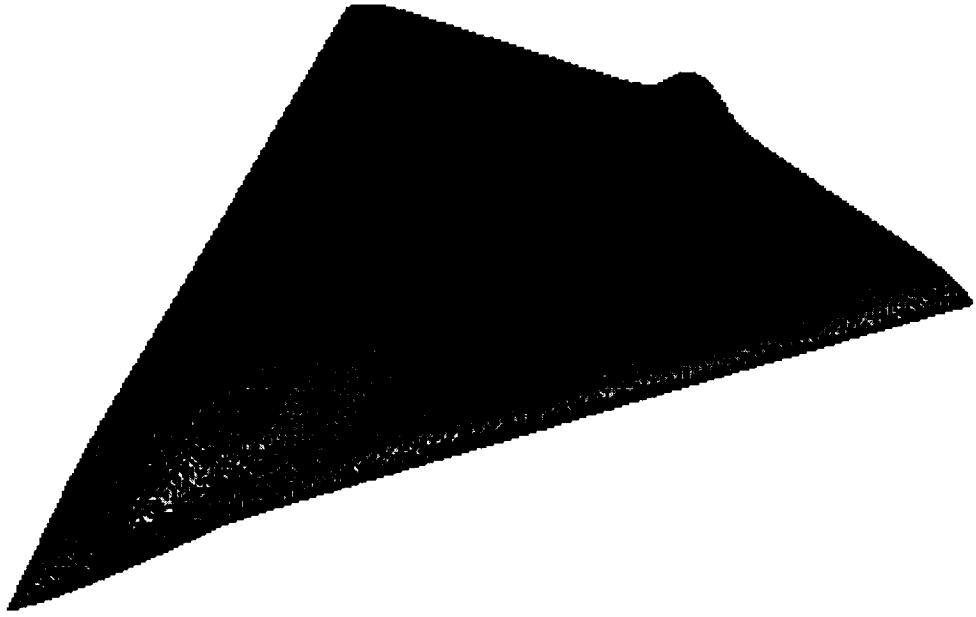

d. Straight Trailing Edge

Figure 3. Concluded

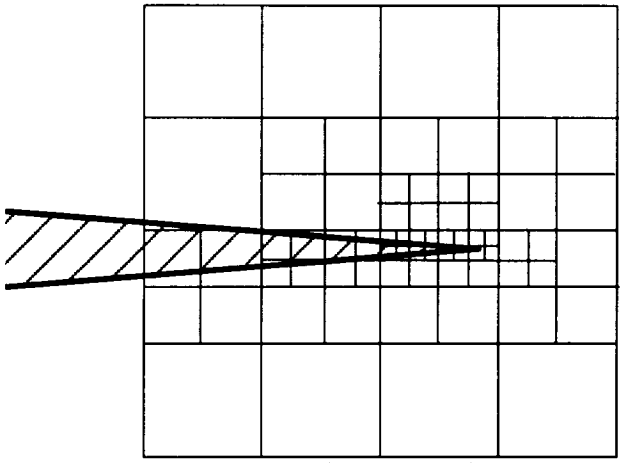

a. Standard Oct–Tree Refinement

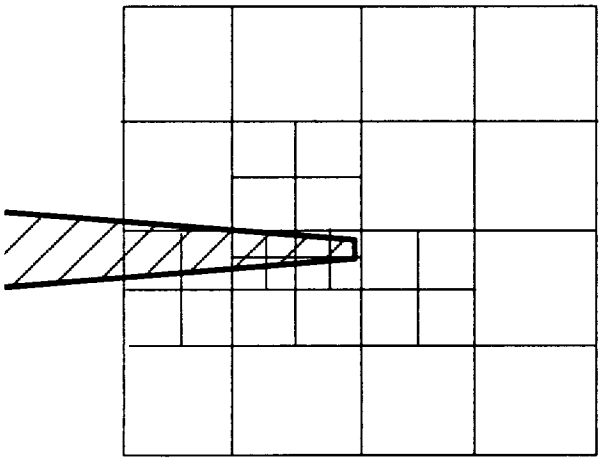

b. Refinement with a Clipped Trailing Edge

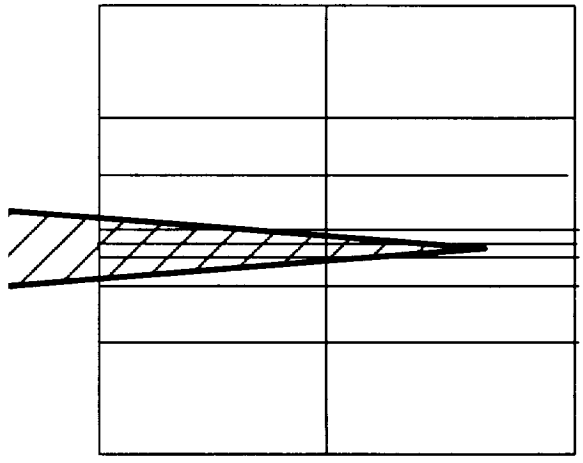

c. Omni–Tree Refinement

Figure 4. Mesh Refinement at the Trailing Edge

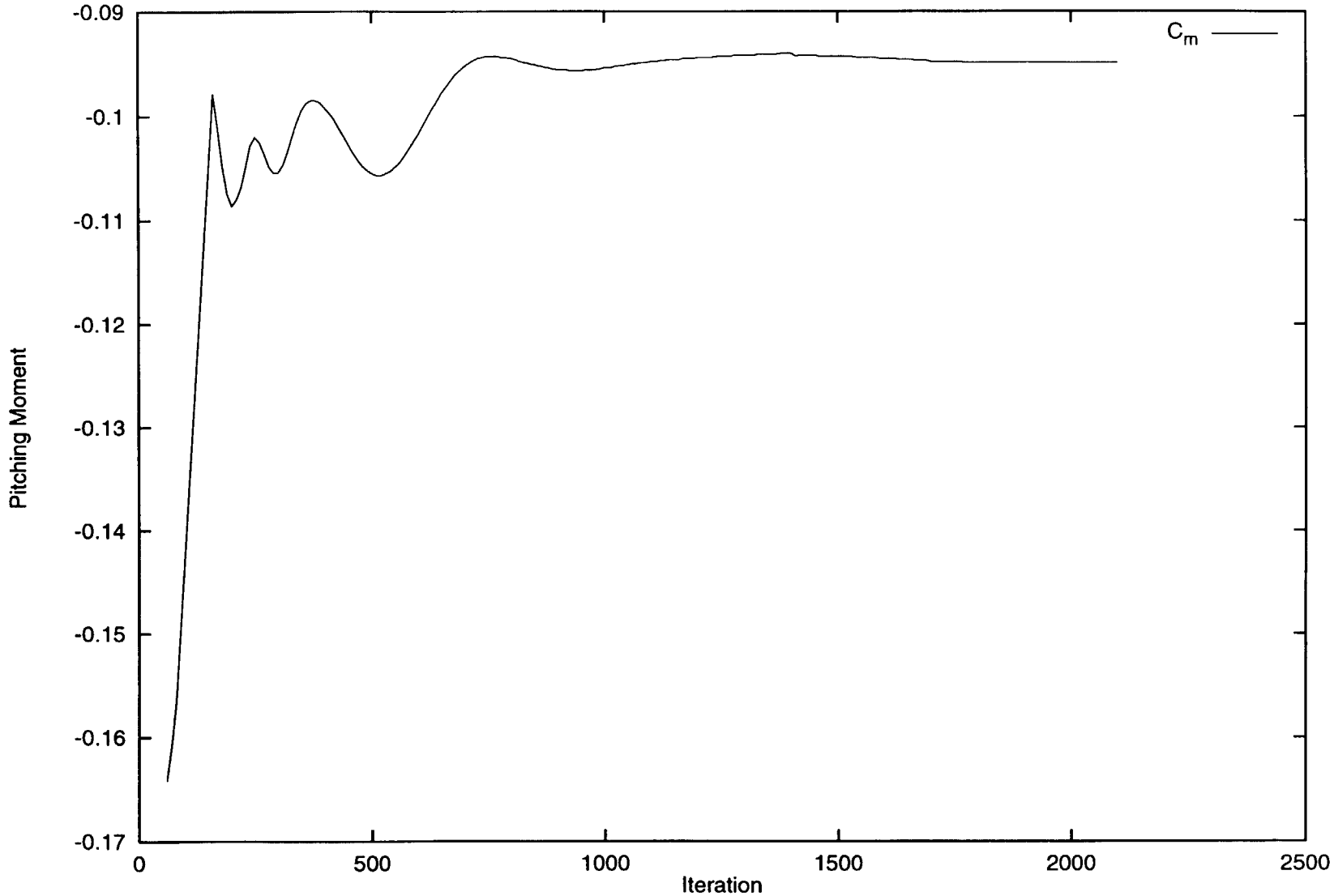

a. Smooth Convergence (Deflected Elevon, M=0.9, α=16)

Figure 5. Convergence Histories

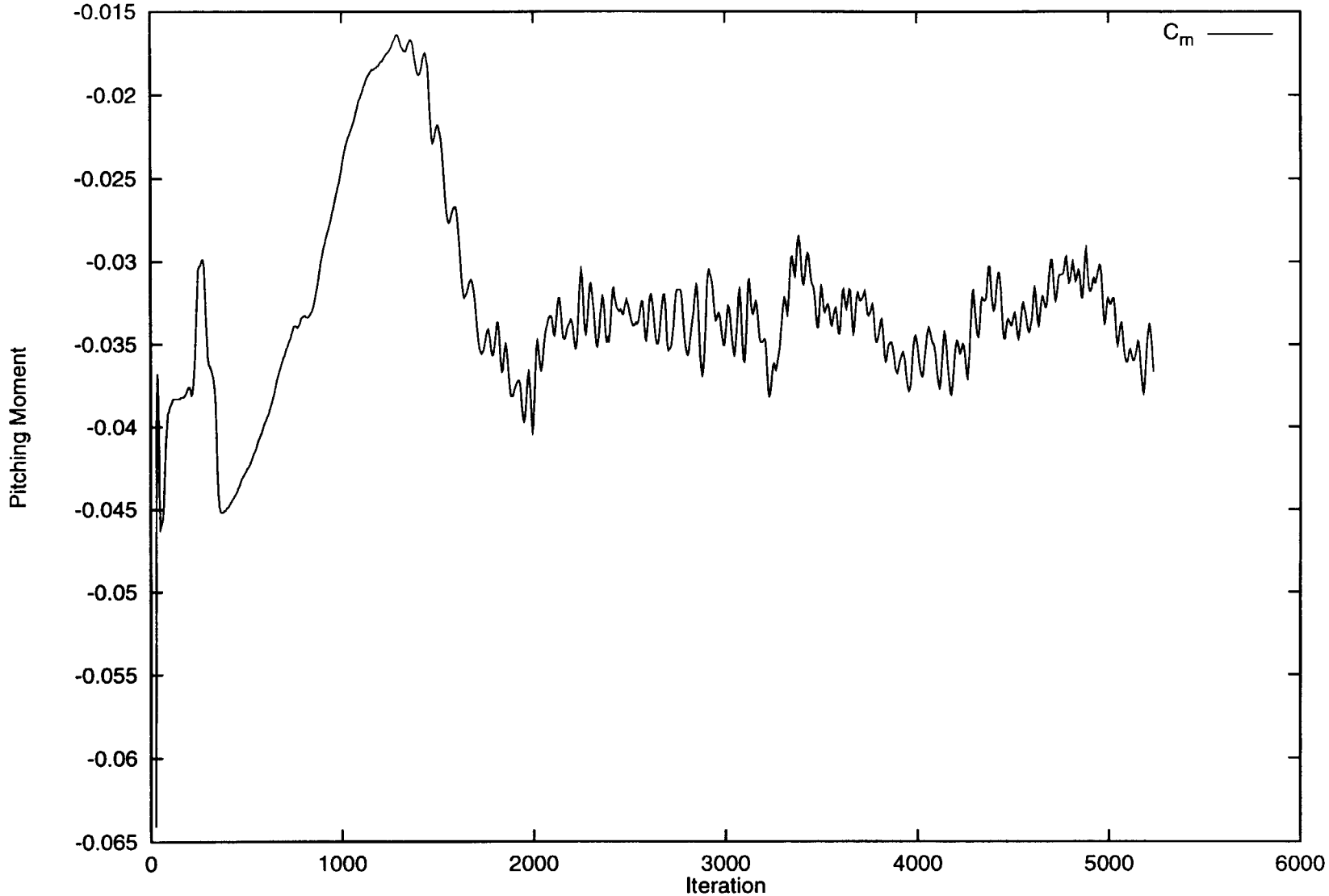

b. Oscillating Convergence (m=0.9, α=20 deg, β=8 deg)

Figure 5. Concluded

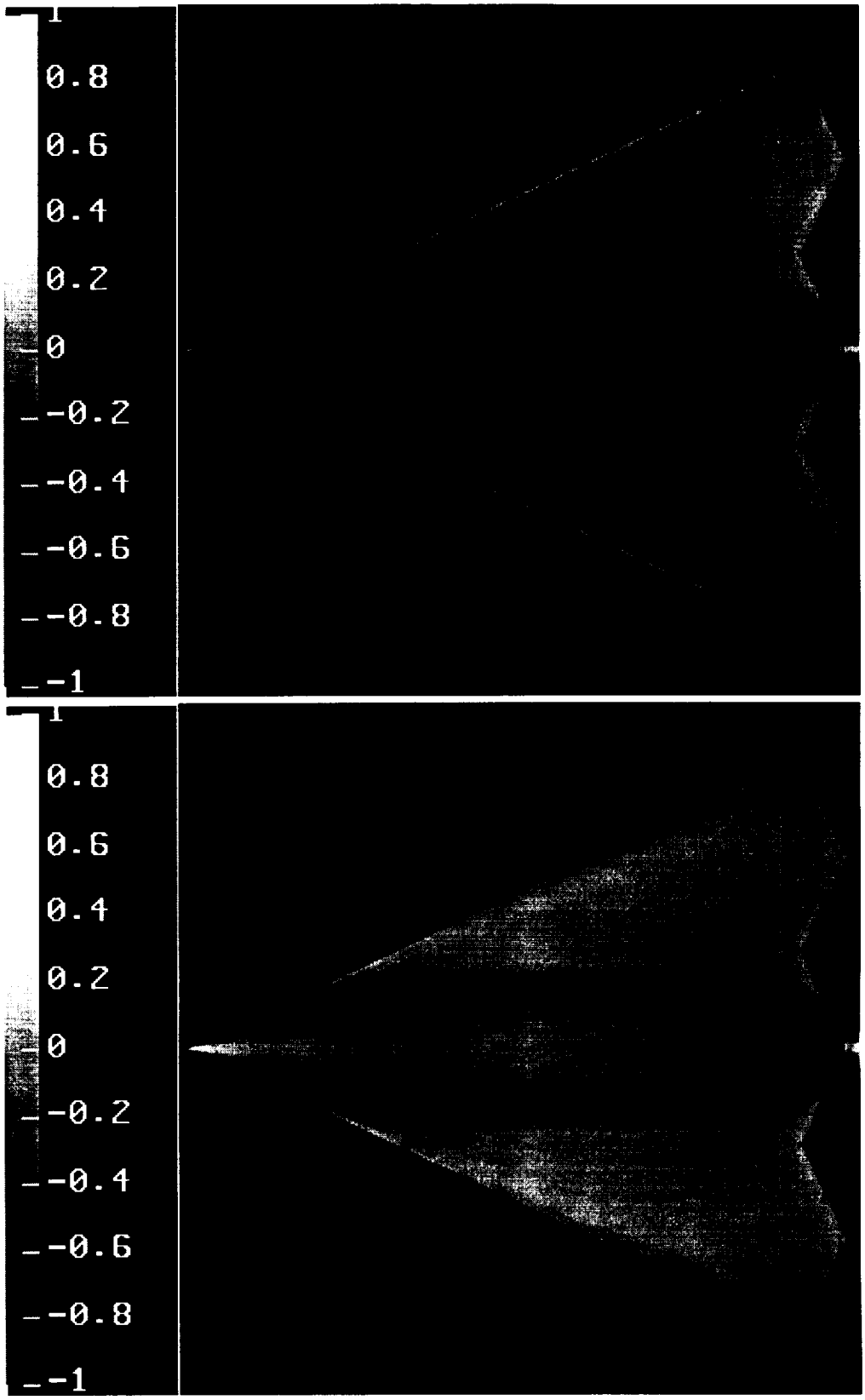

a. Baseline, M=0.6, α=10 deg

Figure 6. Surface C_p Contours for Inviscid Baseline Cases

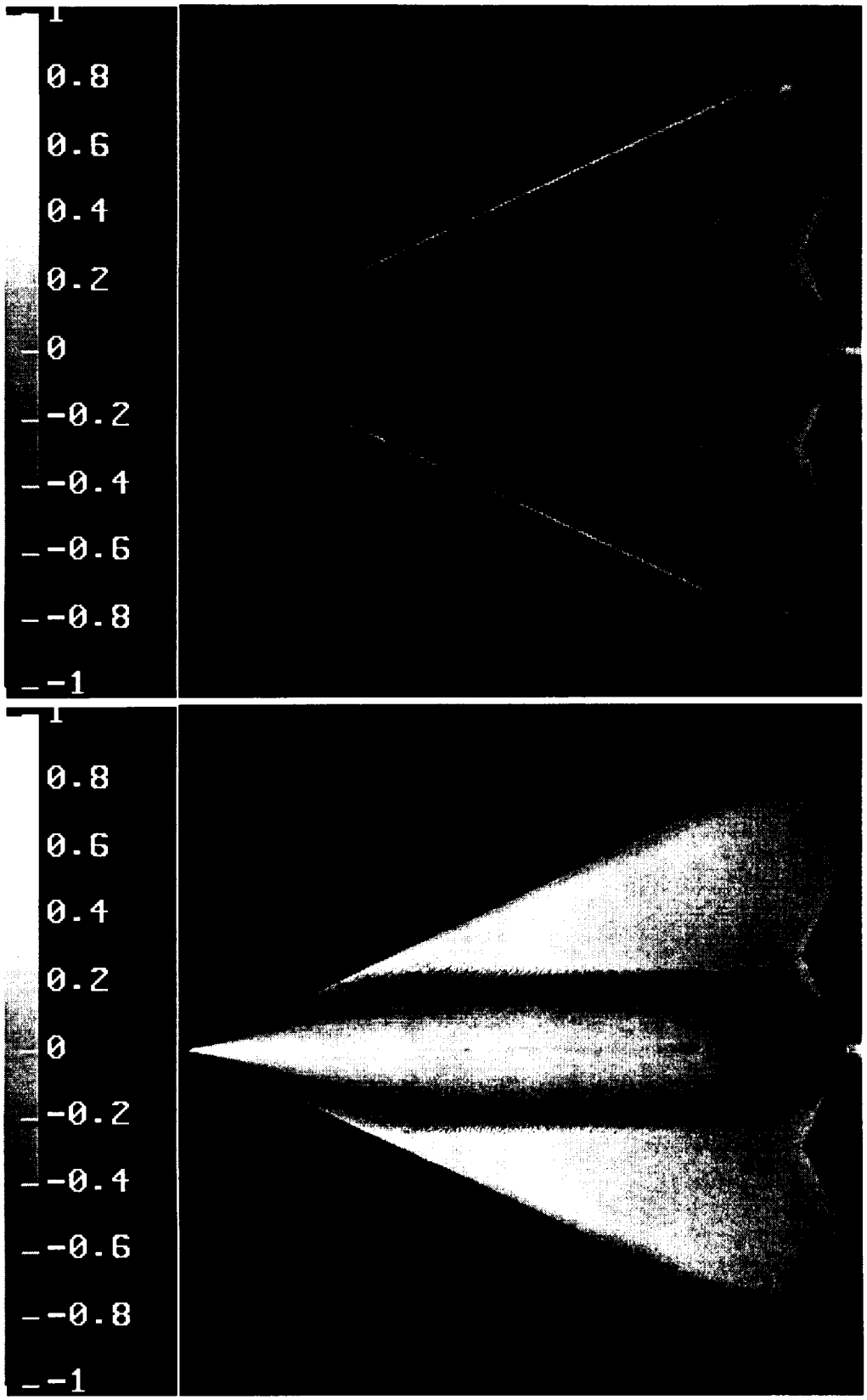

b. Baseline, M=0.6, α=20 deg

Figure 6. Continued

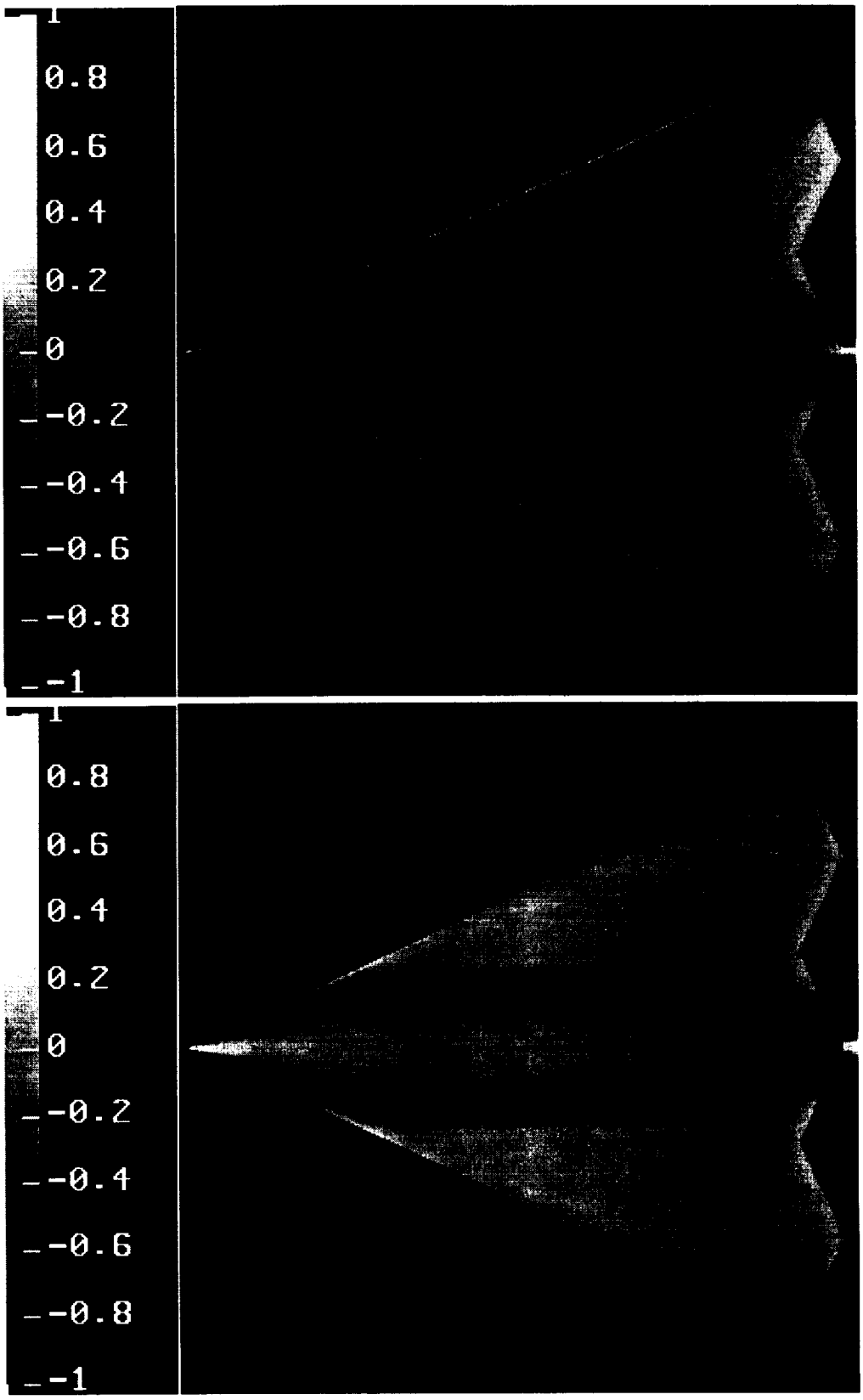

c. Baseline, M=0.9, α=10 deg

Figure 6. Continued

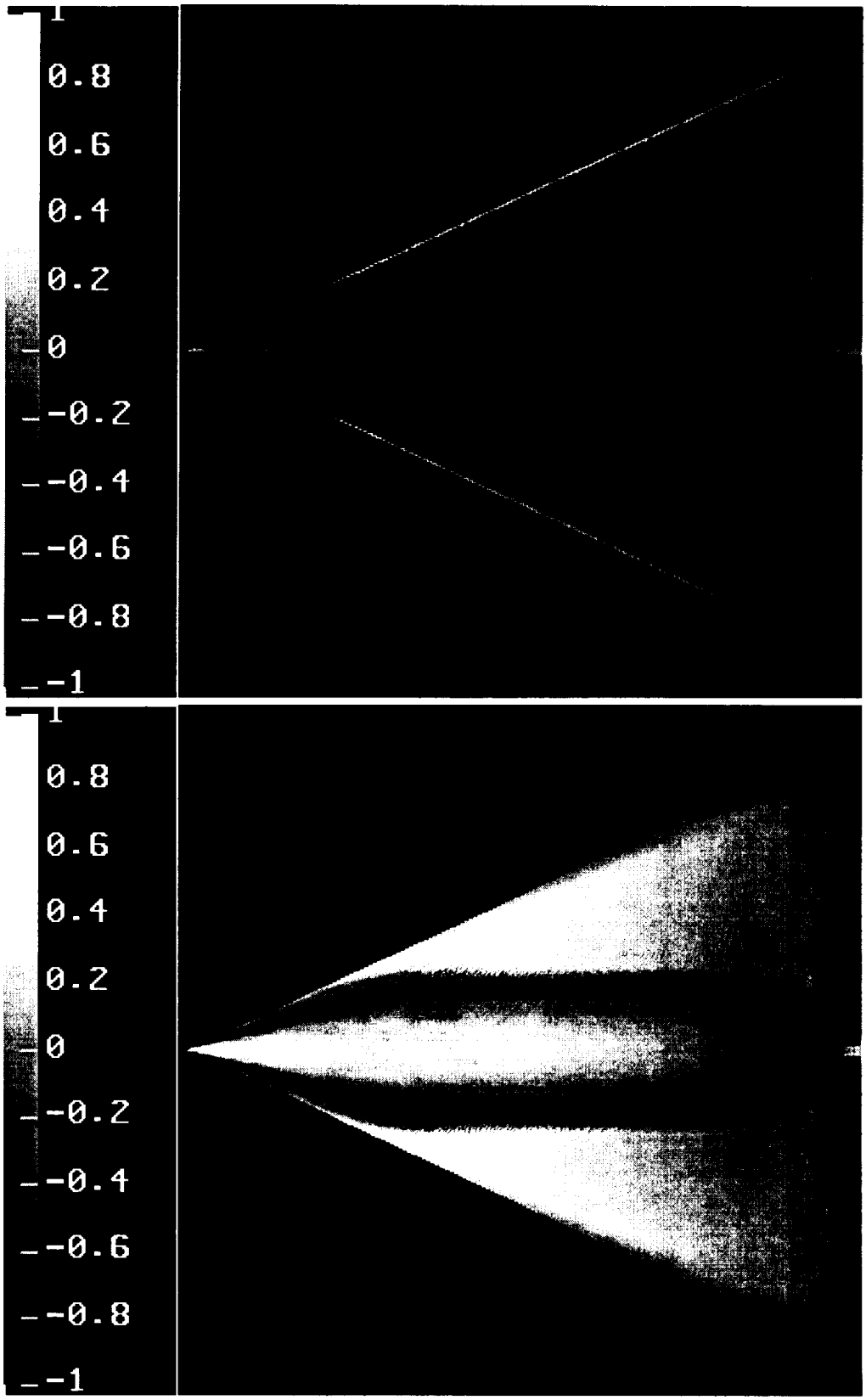

d. Baseline, M=0.9, α=20 deg

Figure 6. Continued

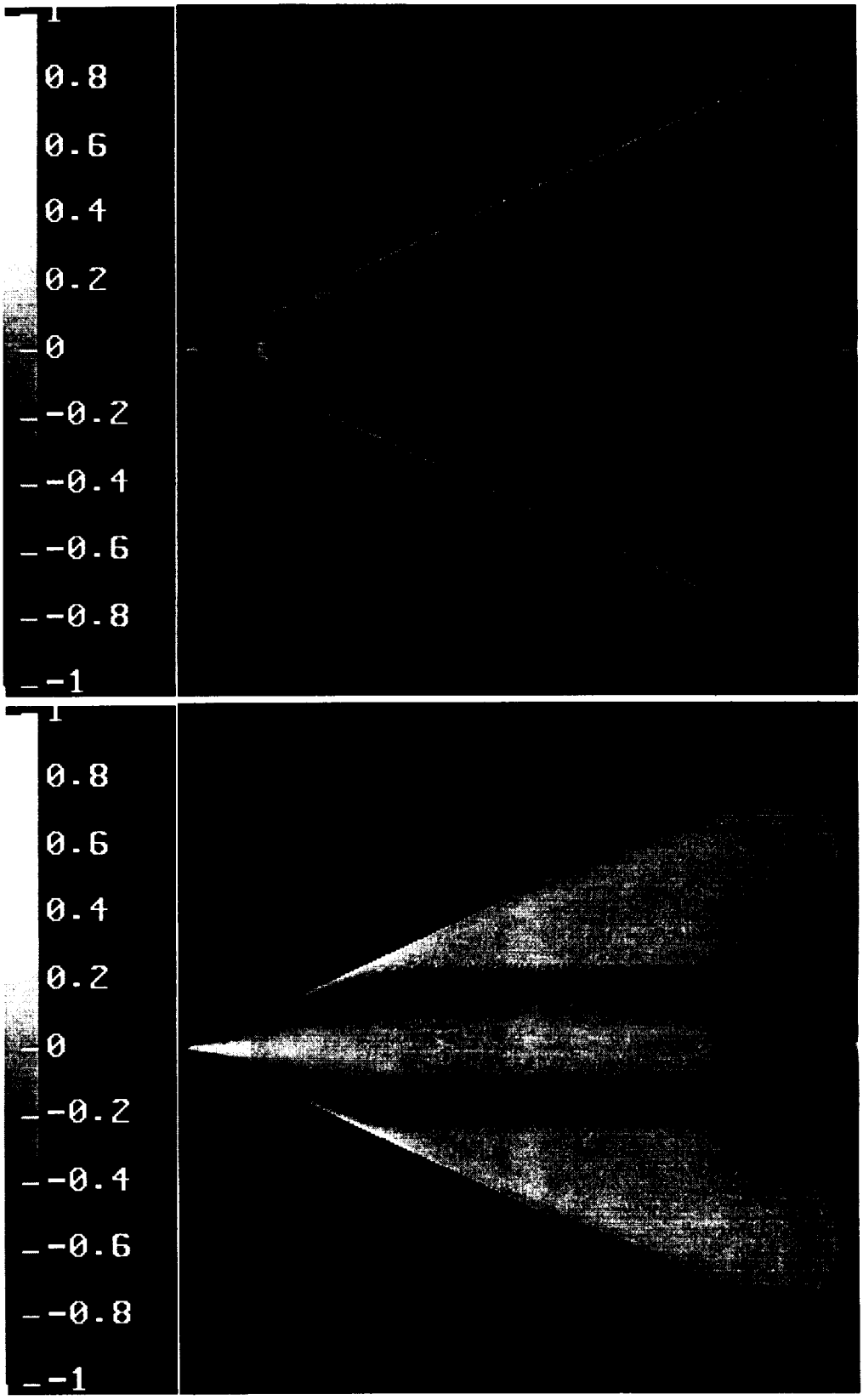

e. Baseline, M=1.2, α=10 deg

Figure 6. Continued

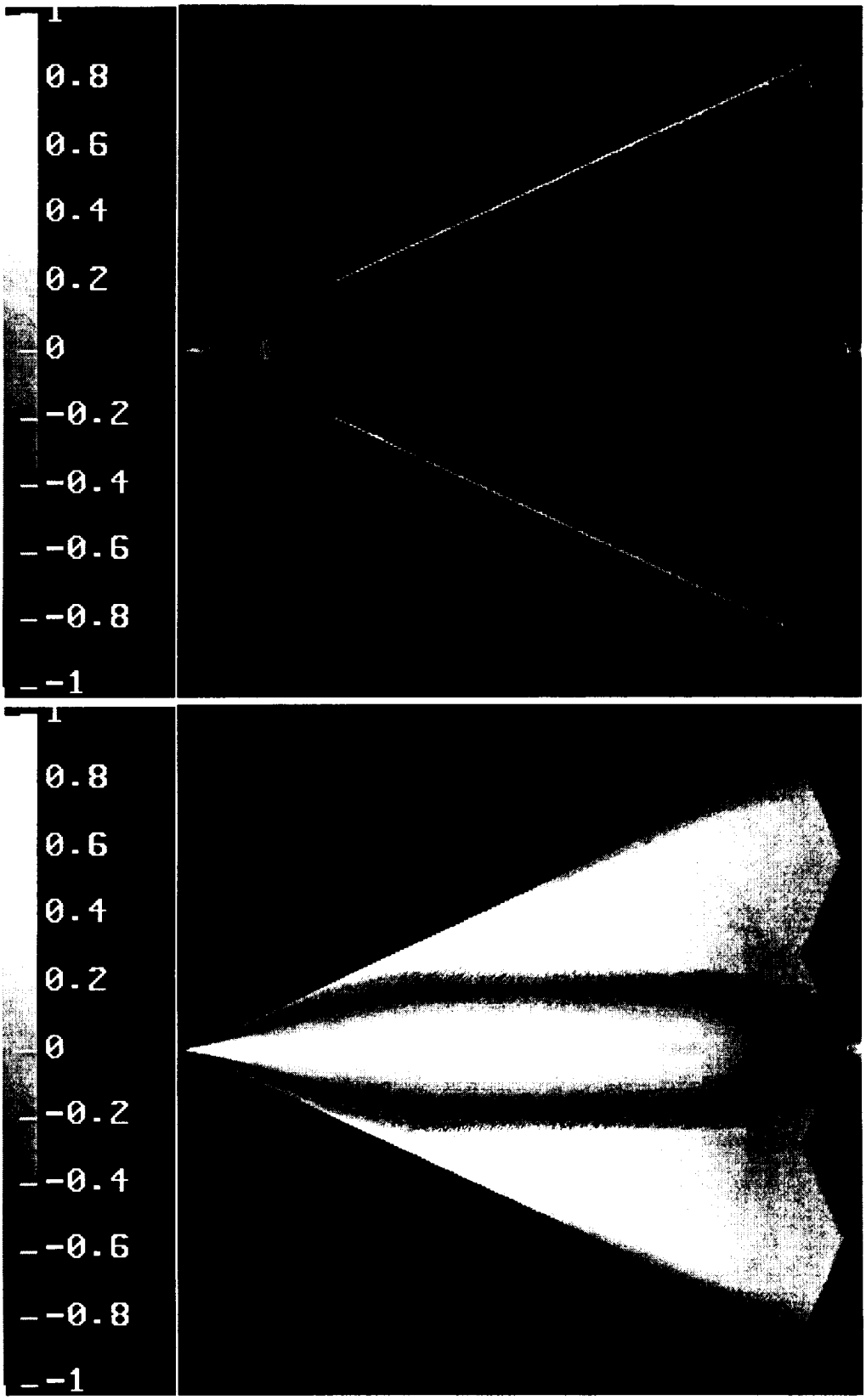

f. Baseline, M=1.2, α=20 deg

Figure 6. Concluded

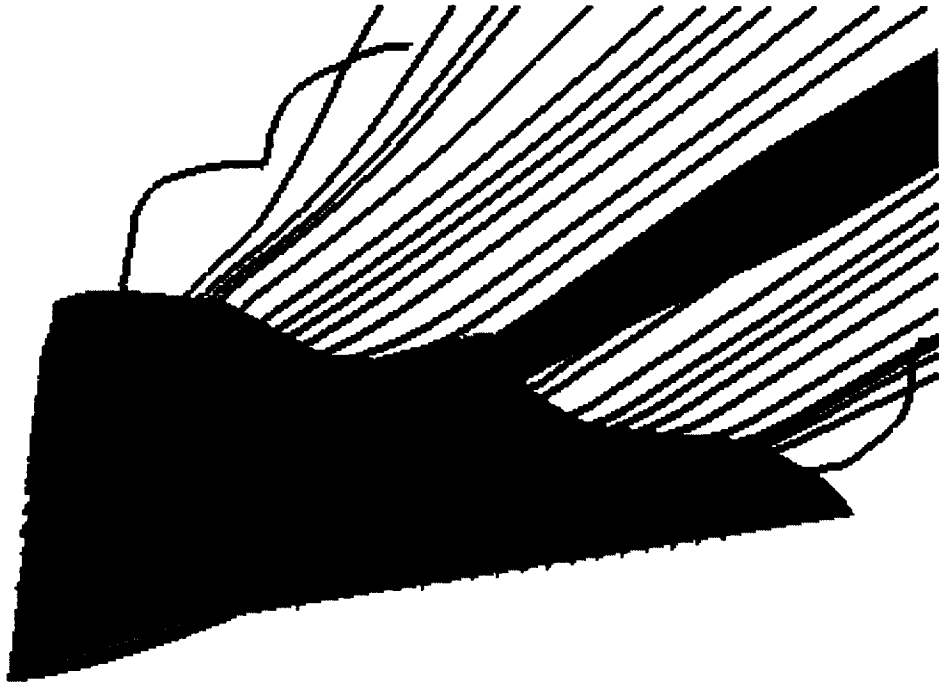

a. Baseline, M=0.6, α=10 deg

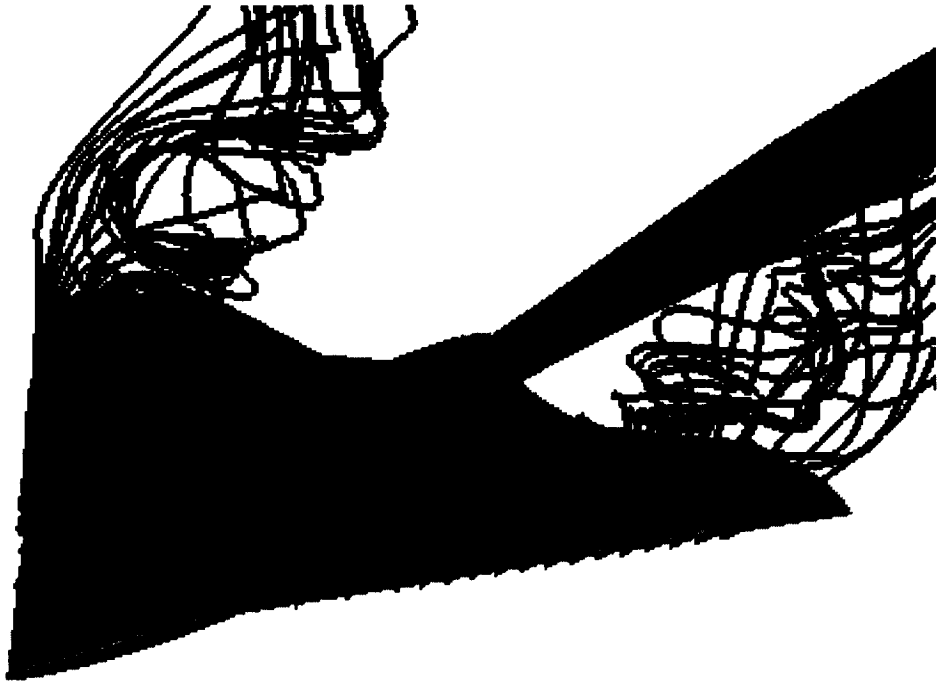

b. Baseline, M=0.6, α=20 deg

Figure 7. Particle Traces for Inviscid Baseline Cases

c. Inviscid Baseline, M=0.9, α=10 deg

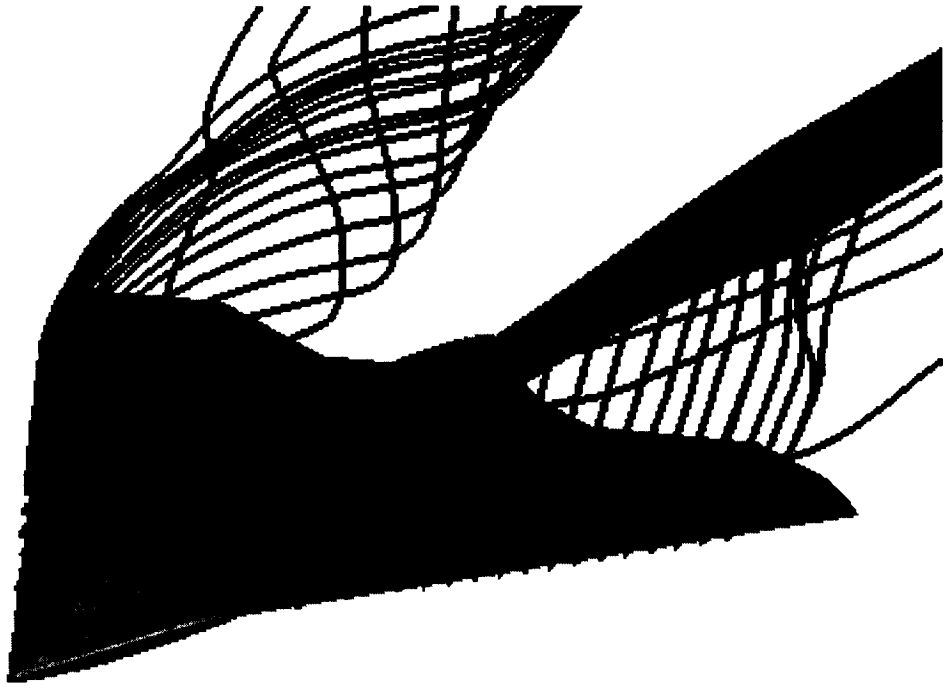

d. Inviscid Baseline, M=0.9, α=20 deg

Figure 7. Continued

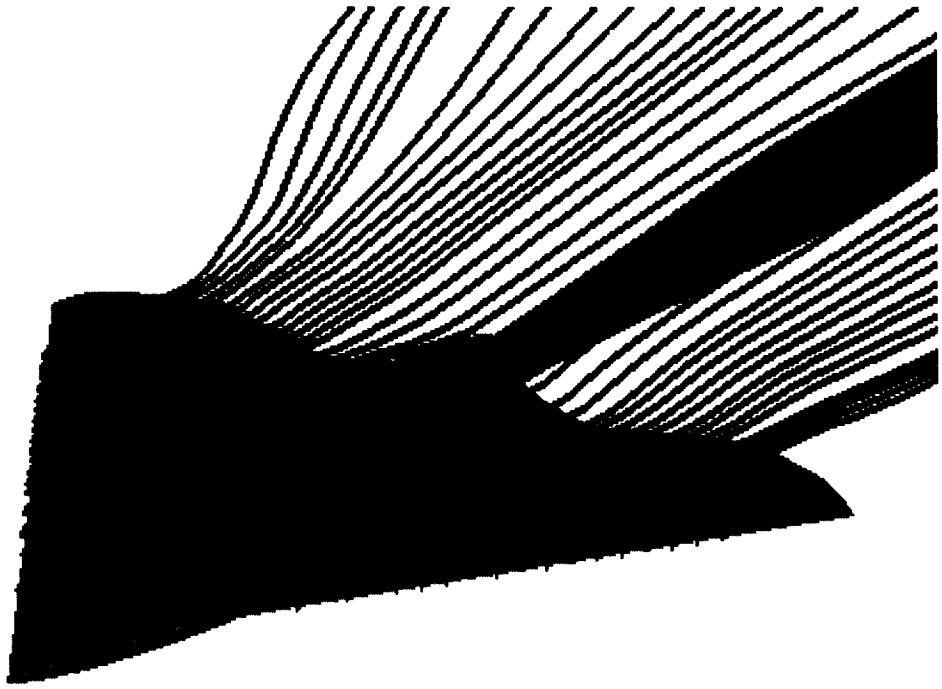

e. Baseline, M=1.2, α=10 deg

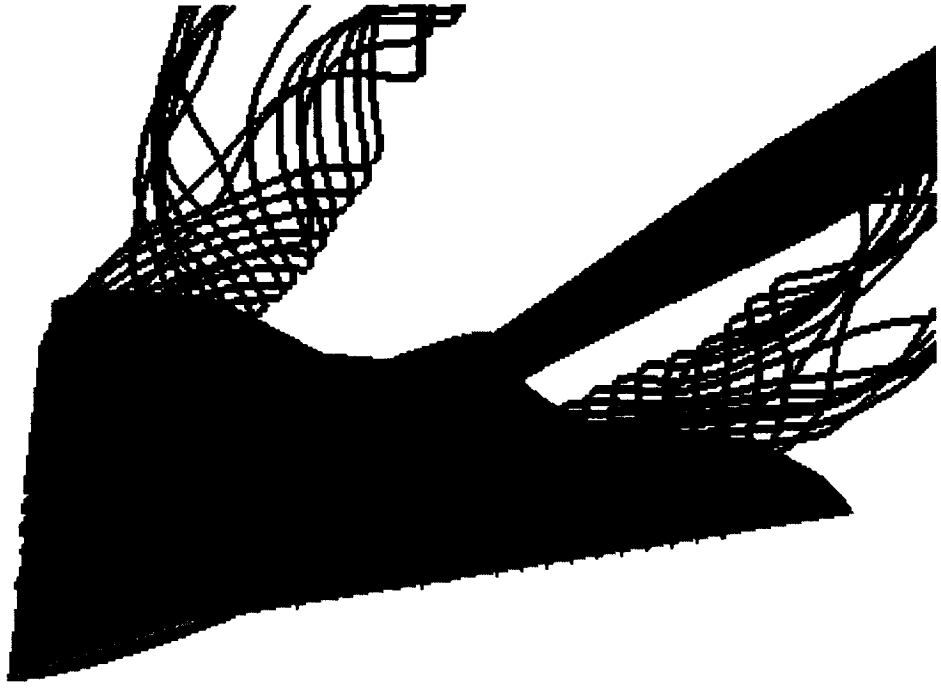

f. Baseline, M=1.2, α=20 deg

Figure 7. Concluded

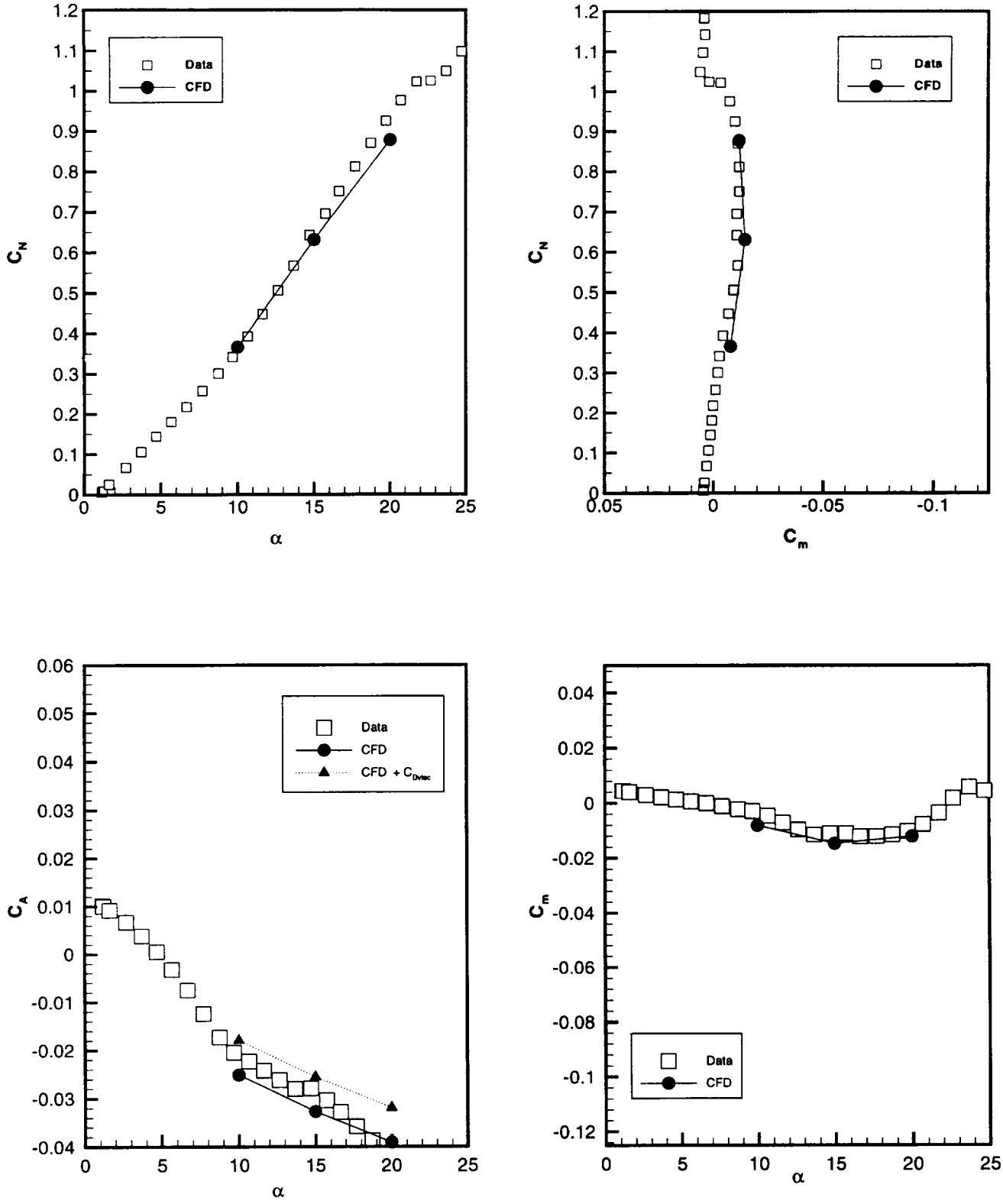

a. Inviscid Baseline Case, M=0.6

Figure 8. Integrated Load Comparisons for Inviscid Baseline Cases

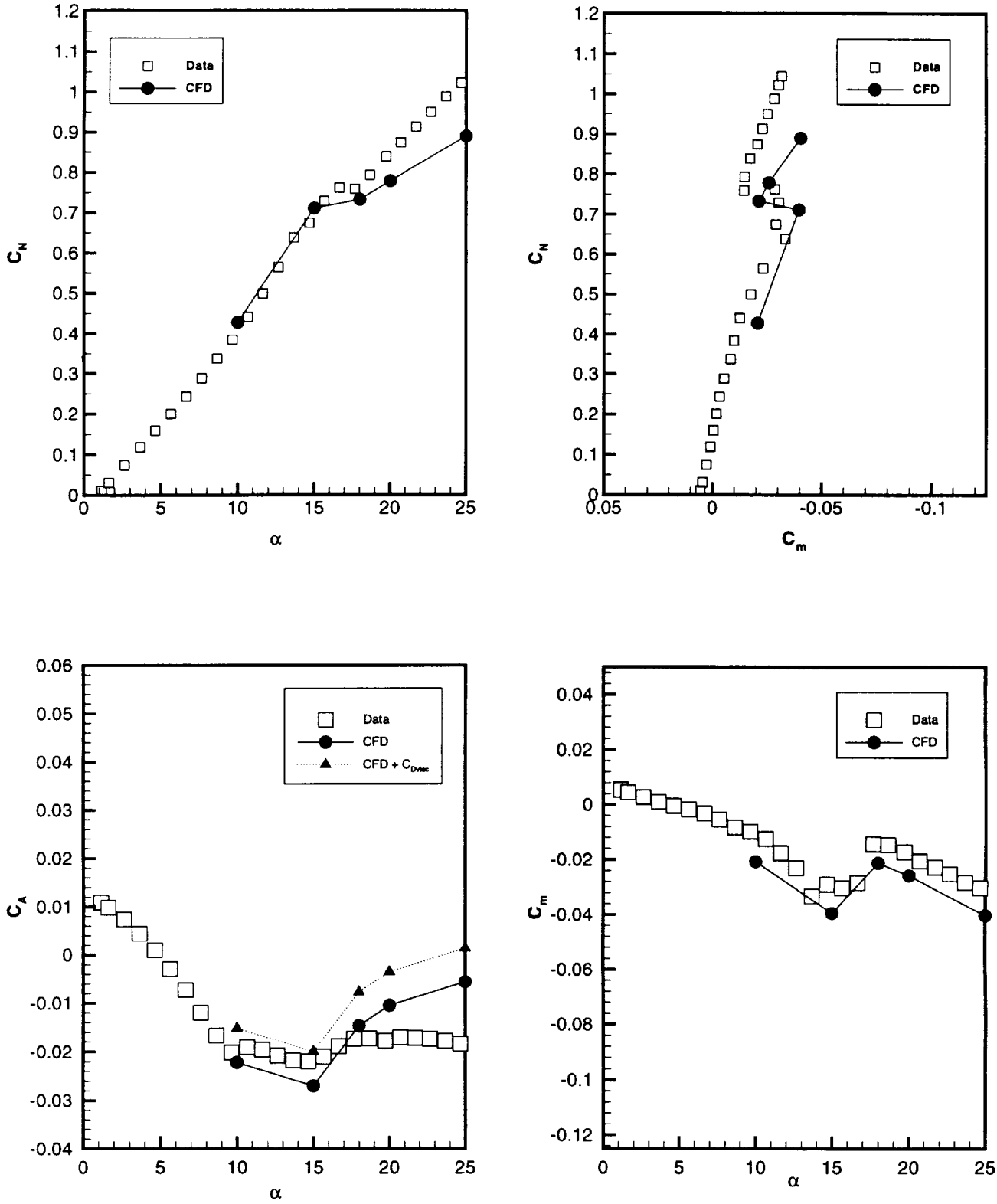

b. Inviscid Baseline Case, M=0.90
Figure 8. Continued

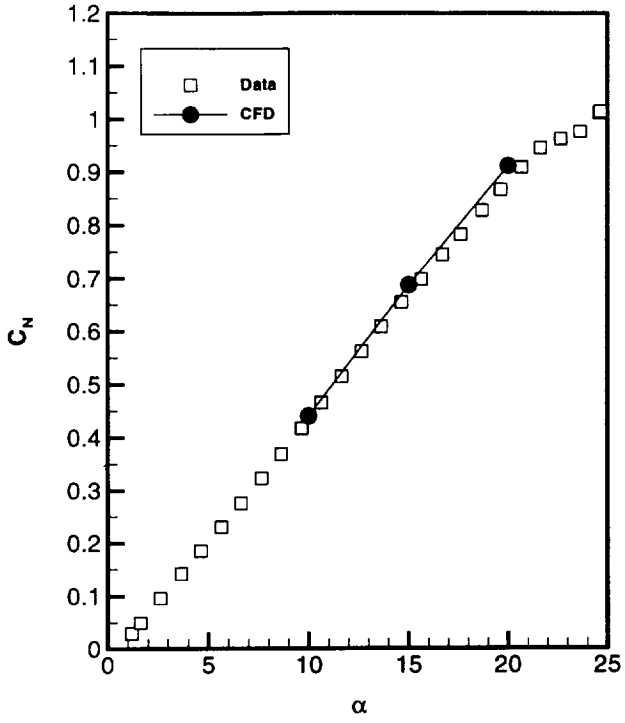

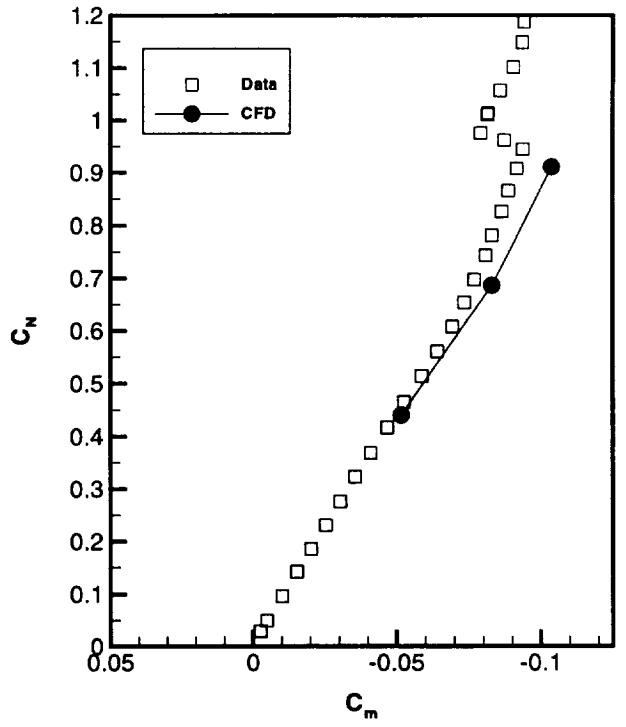

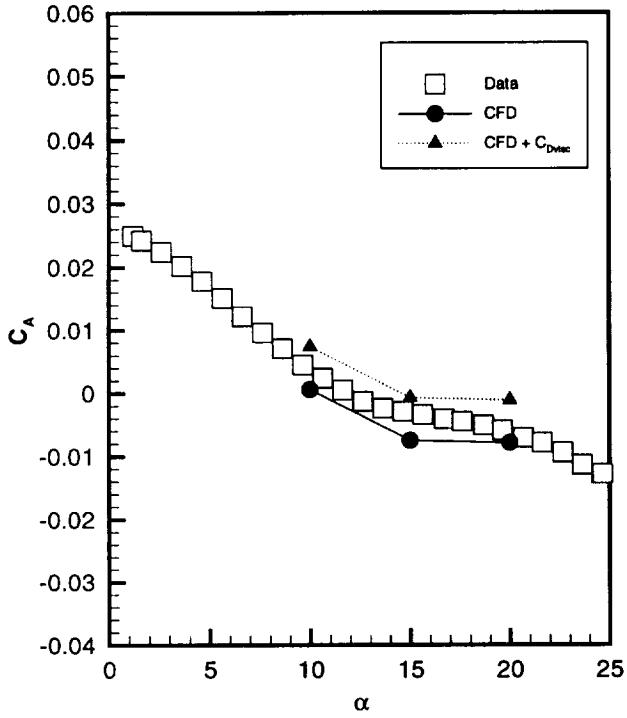

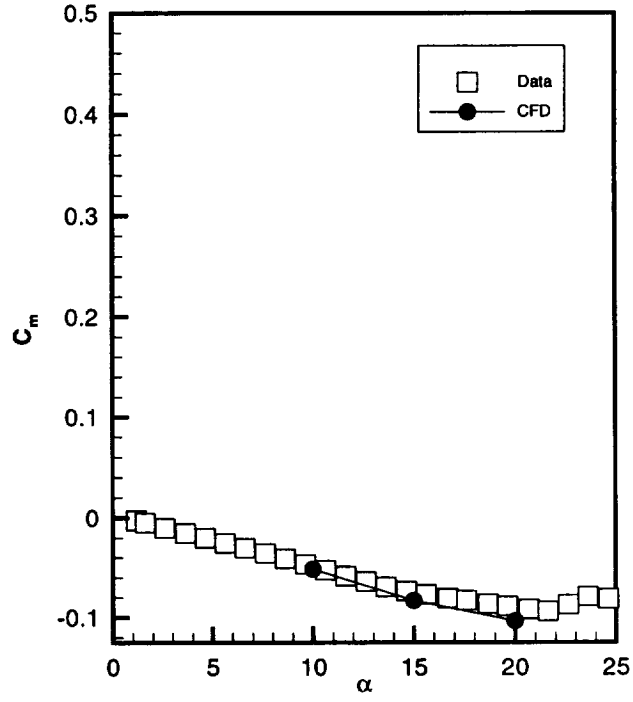

c. Inviscid Baseline Case, M=1.20
Figure 8. Concluded

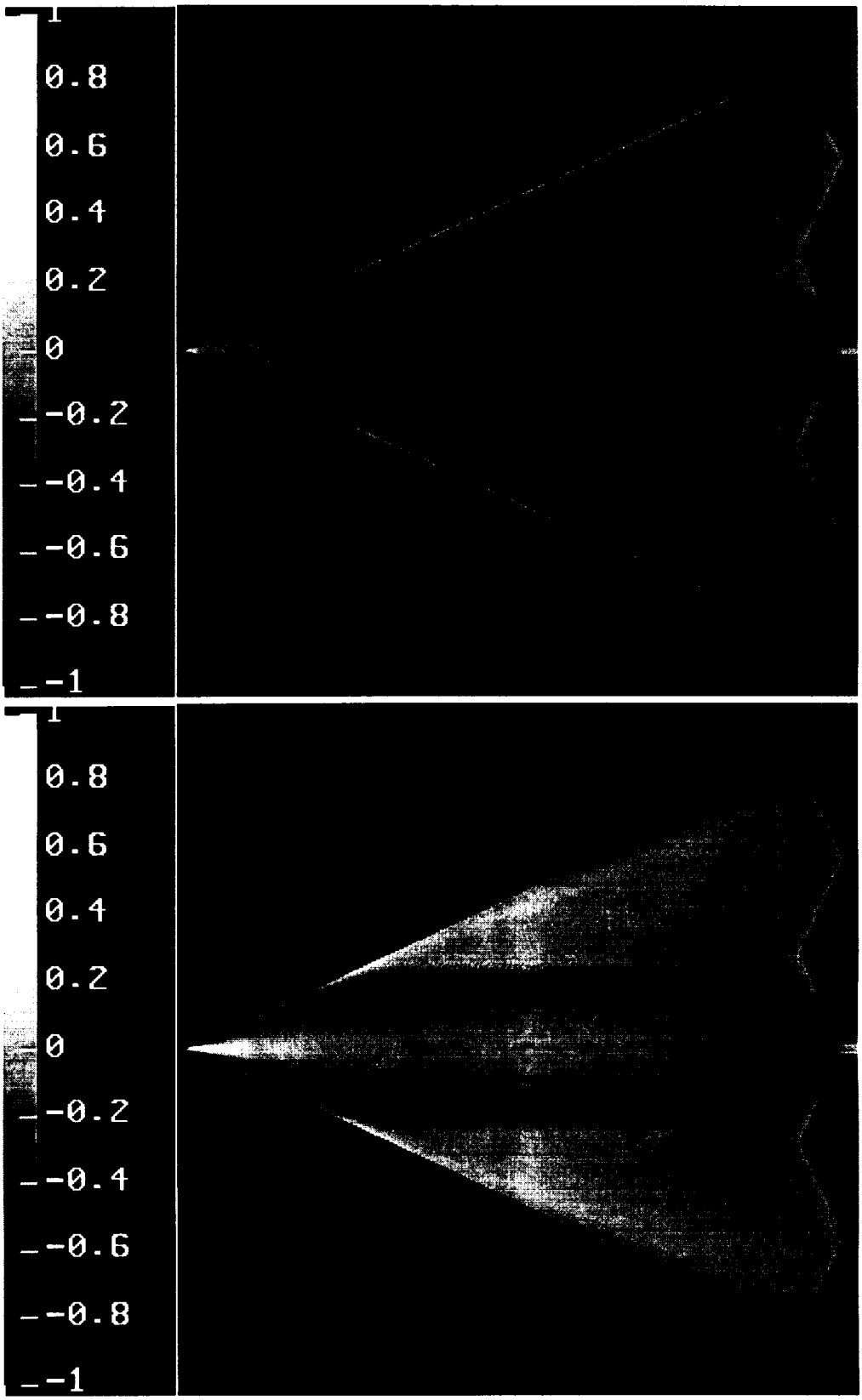

a. Viscous Baseline, M=0.9, α=10 deg

Figure 9. Surface C_p Contours for Viscous Baseline Cases, M = 0.9

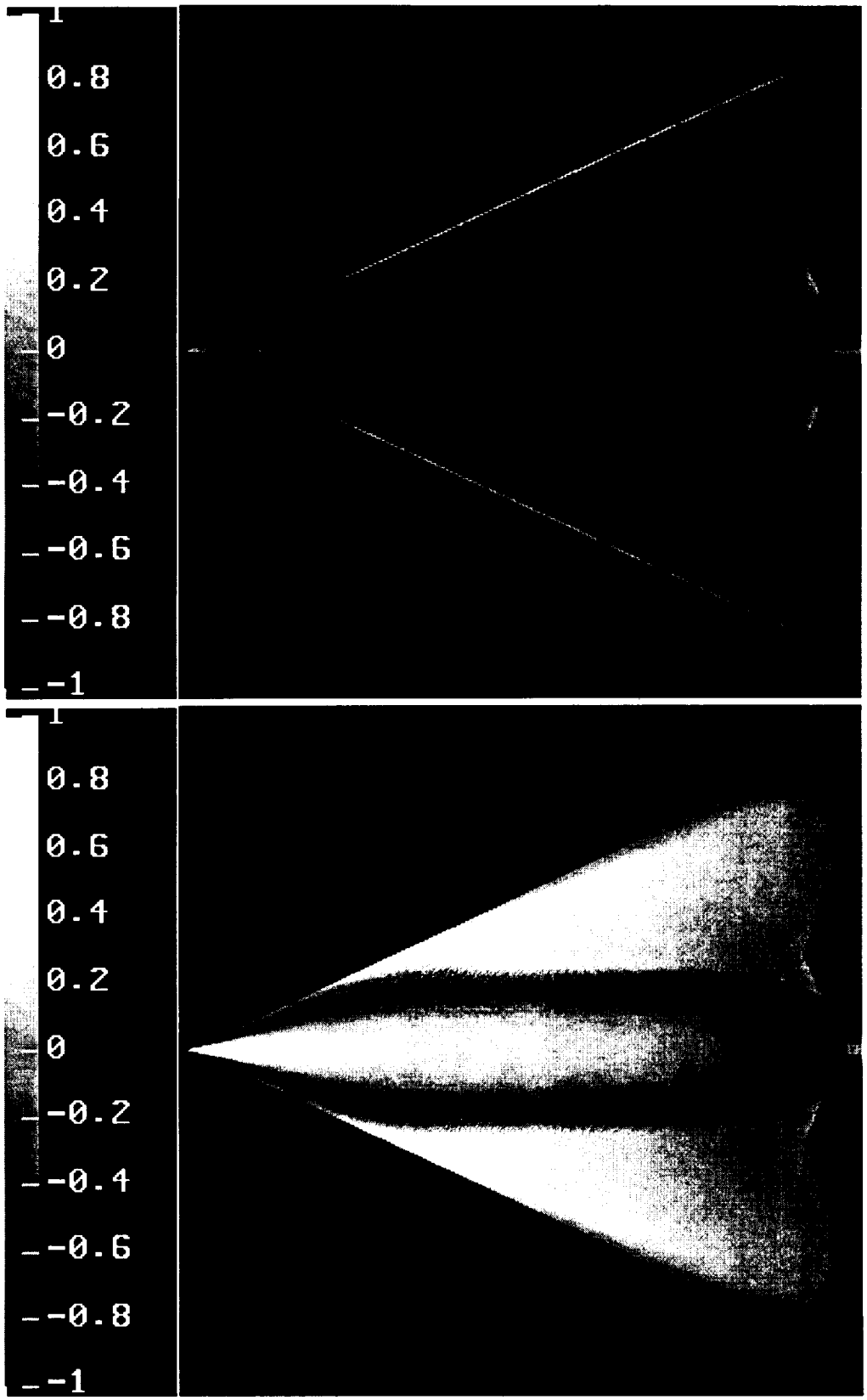

b. Viscous Baseline, M=0.9, α=20 deg

Figure 9. Concluded

a. Inviscid Baseline, M=0.9, α=10 deg

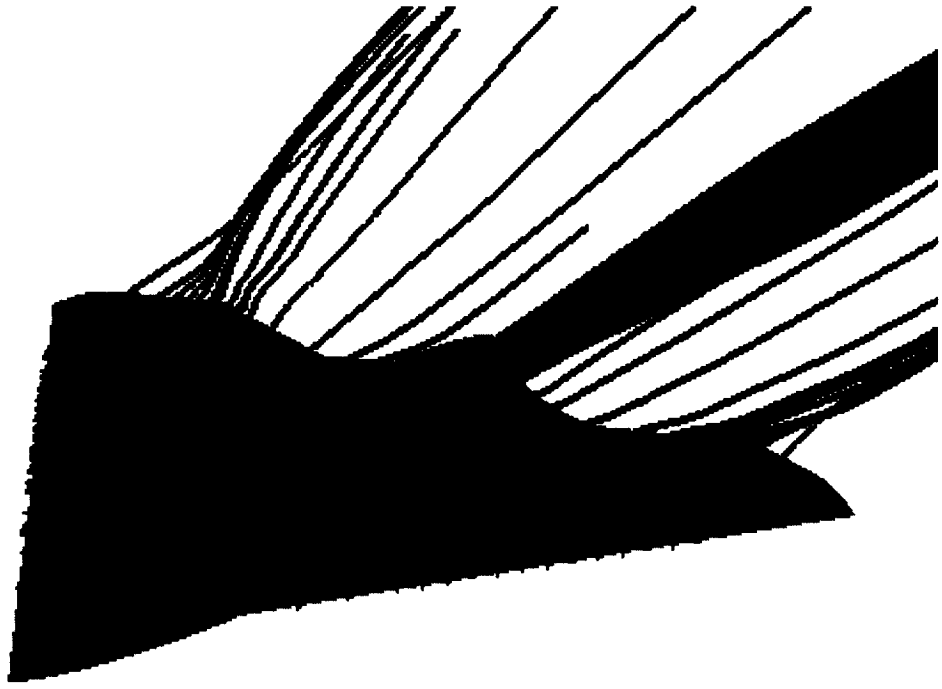

b. Viscous Baseline, M=0.9, α=10 deg

Figure 10. Particle Traces for Inviscid and Viscous Baseline Cases, M = 0.9

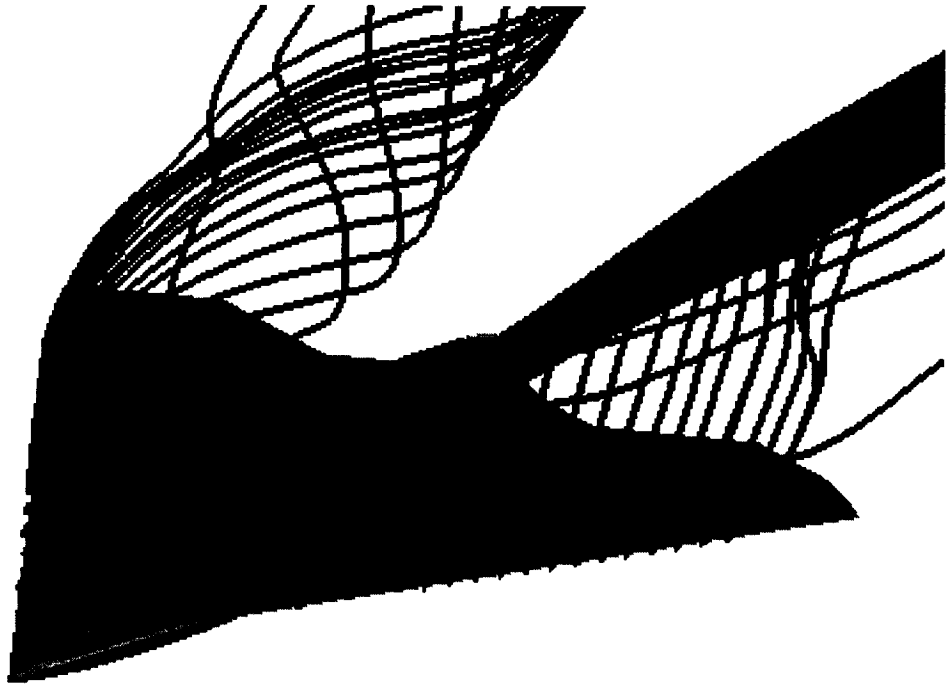

c. Inviscid Baseline, M=0.9, α=20 deg

d. Viscous Baseline, M=0.9, α=20 deg

Figure 10. Concluded

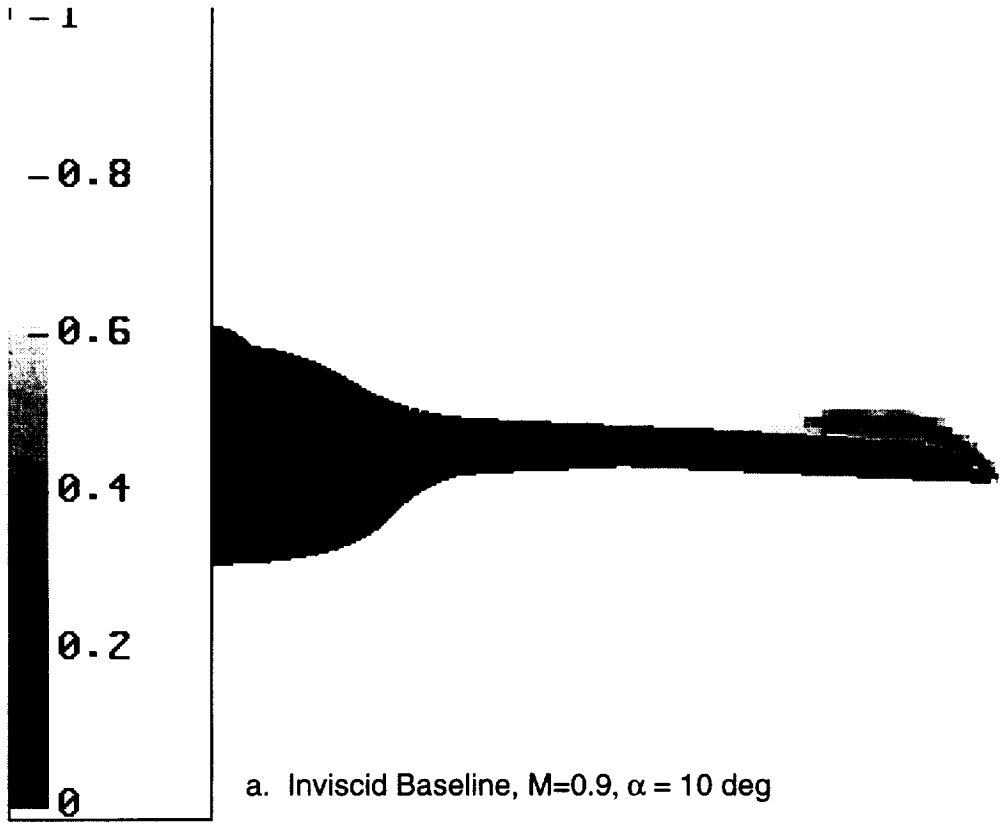

a. Inviscid Baseline, M=0.9, α = 10 deg

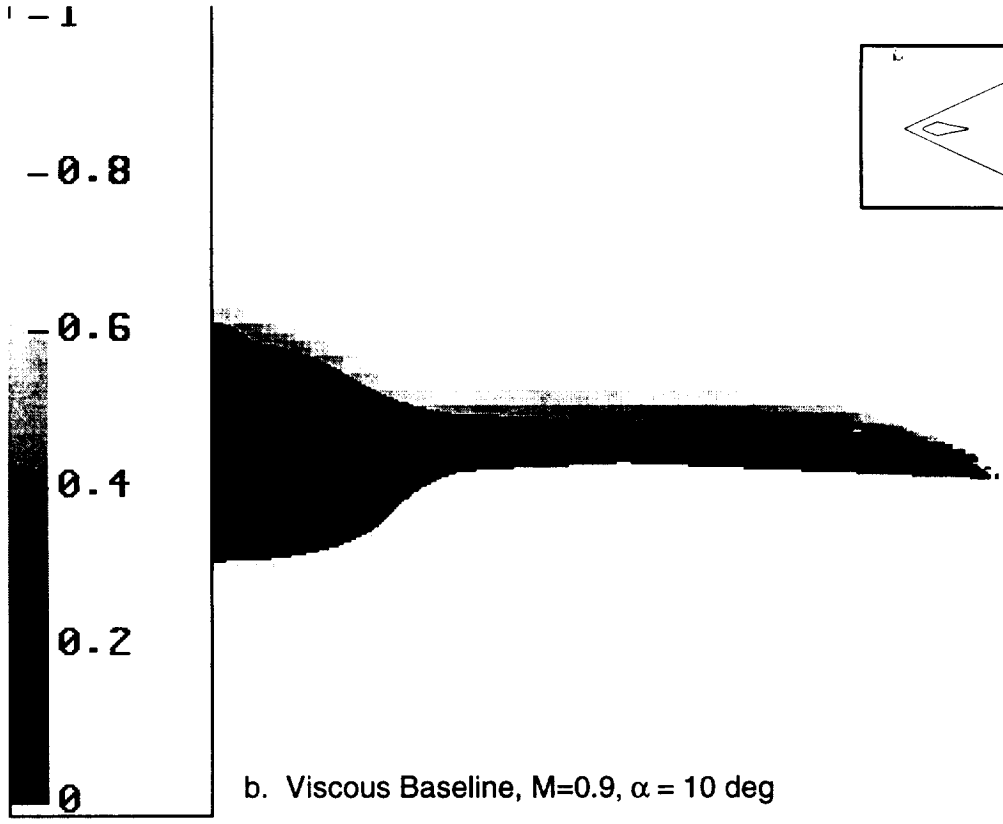

b. Viscous Baseline, M=0.9, α = 10 deg

Figure 11. Normalized Stagnation Pressure Contours for Viscous and Inviscid Baseline Cases, M = 0.9, X=2.0 ft.

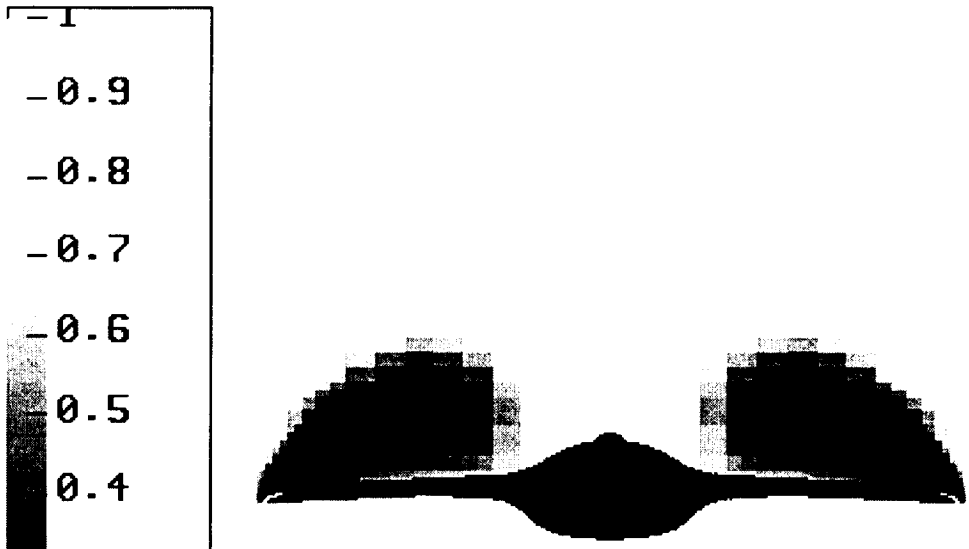

c. Inviscid Baseline, M=0.9, α = 20 deg

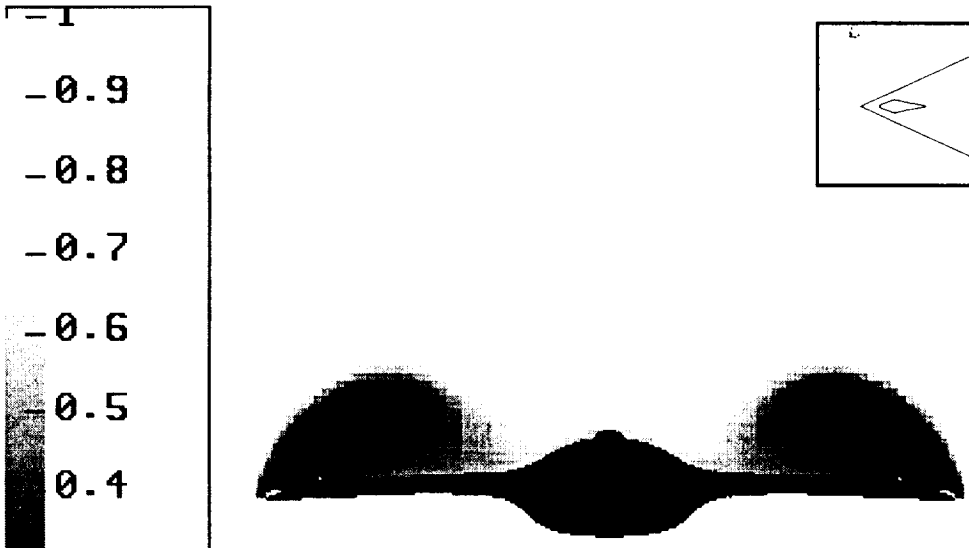

d. Viscous Baseline, M=0.9, α = 20 deg

Figure 11. Concluded

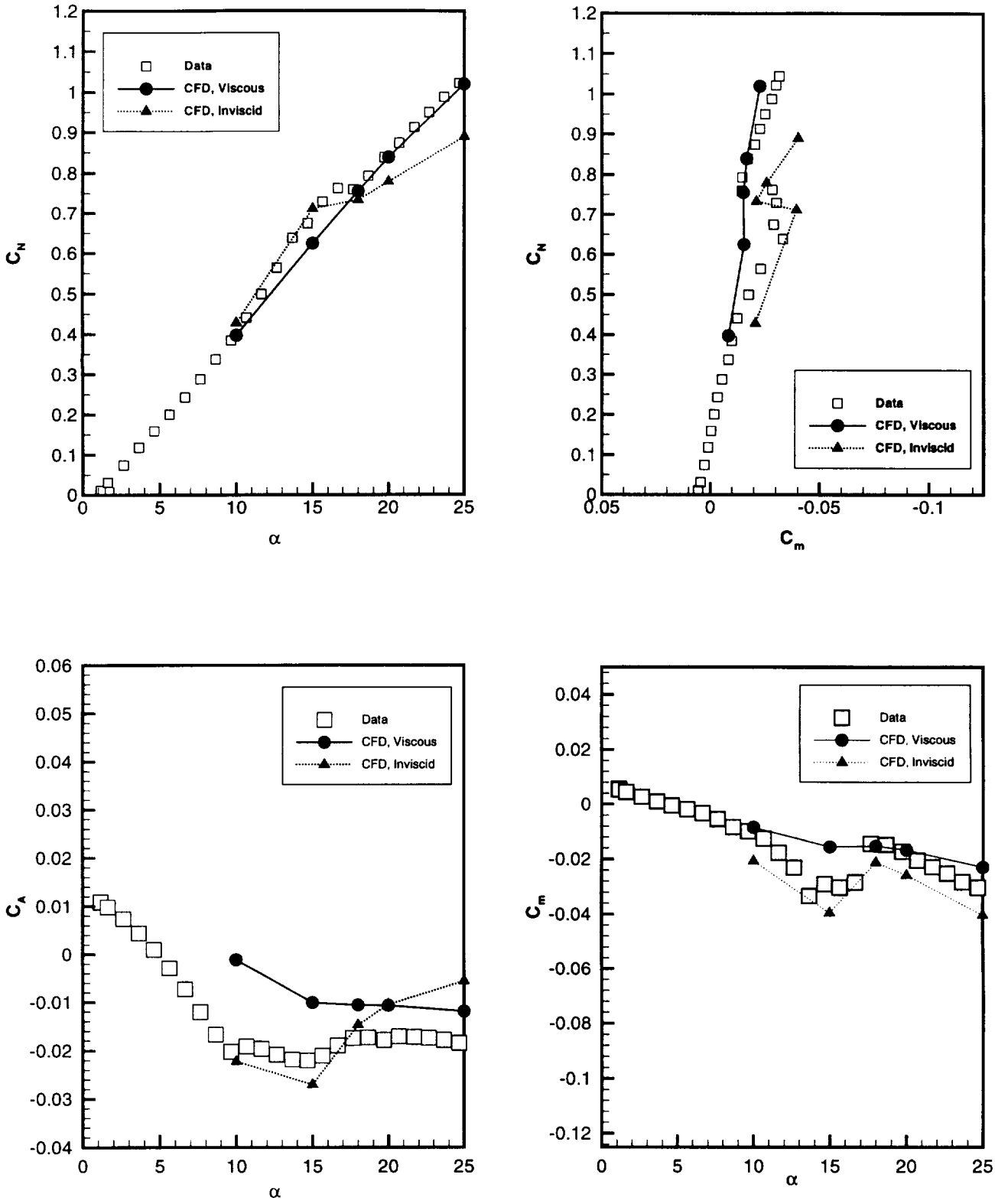

Figure 12. Integrated Load Comparisons for Viscous Baseline Case, M=0.90

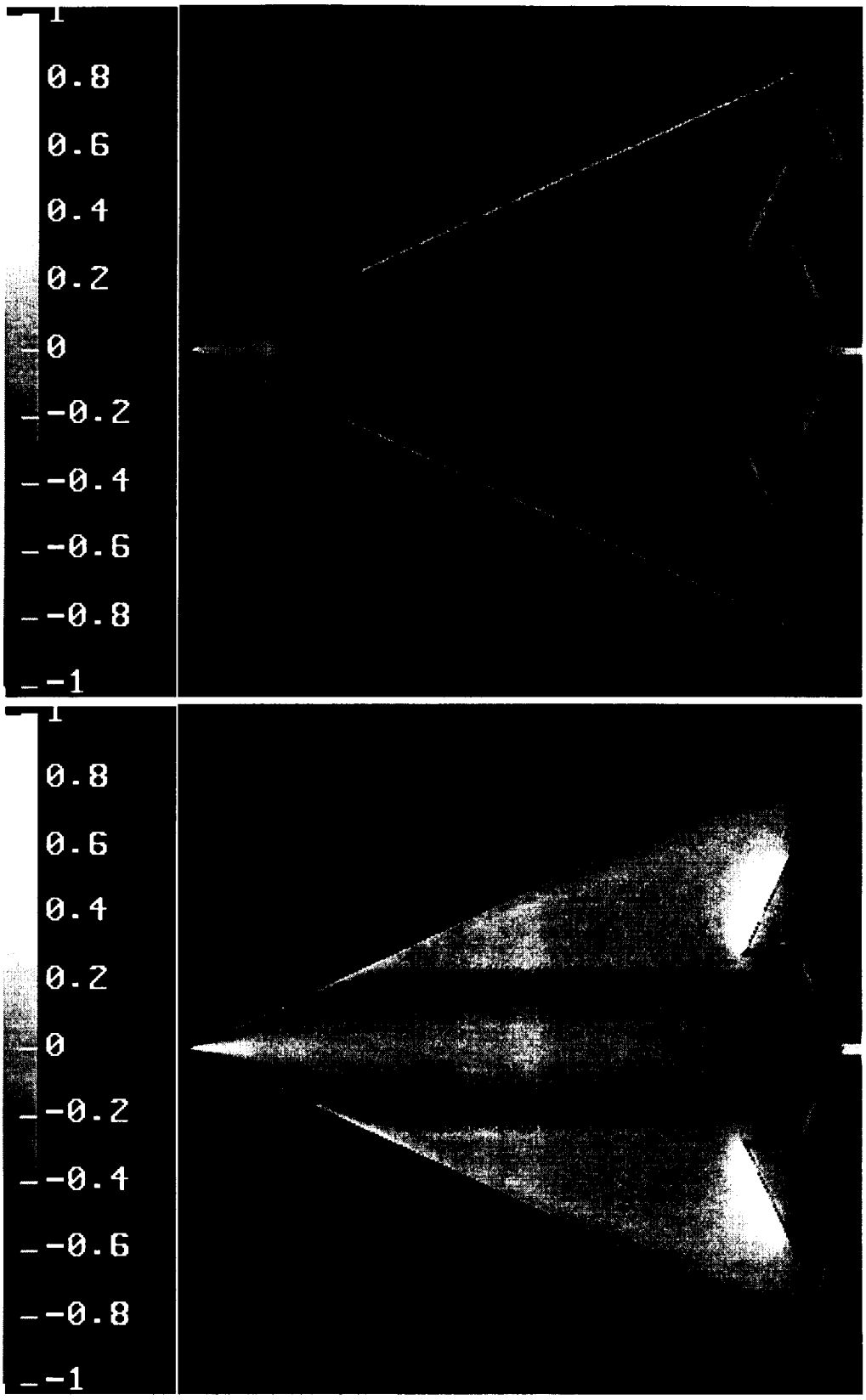

a. Deflected Elevon, M=0.9, α=10 deg

Figure 13. Surface C_p Contours for Deflected Control Cases, M = 0.9

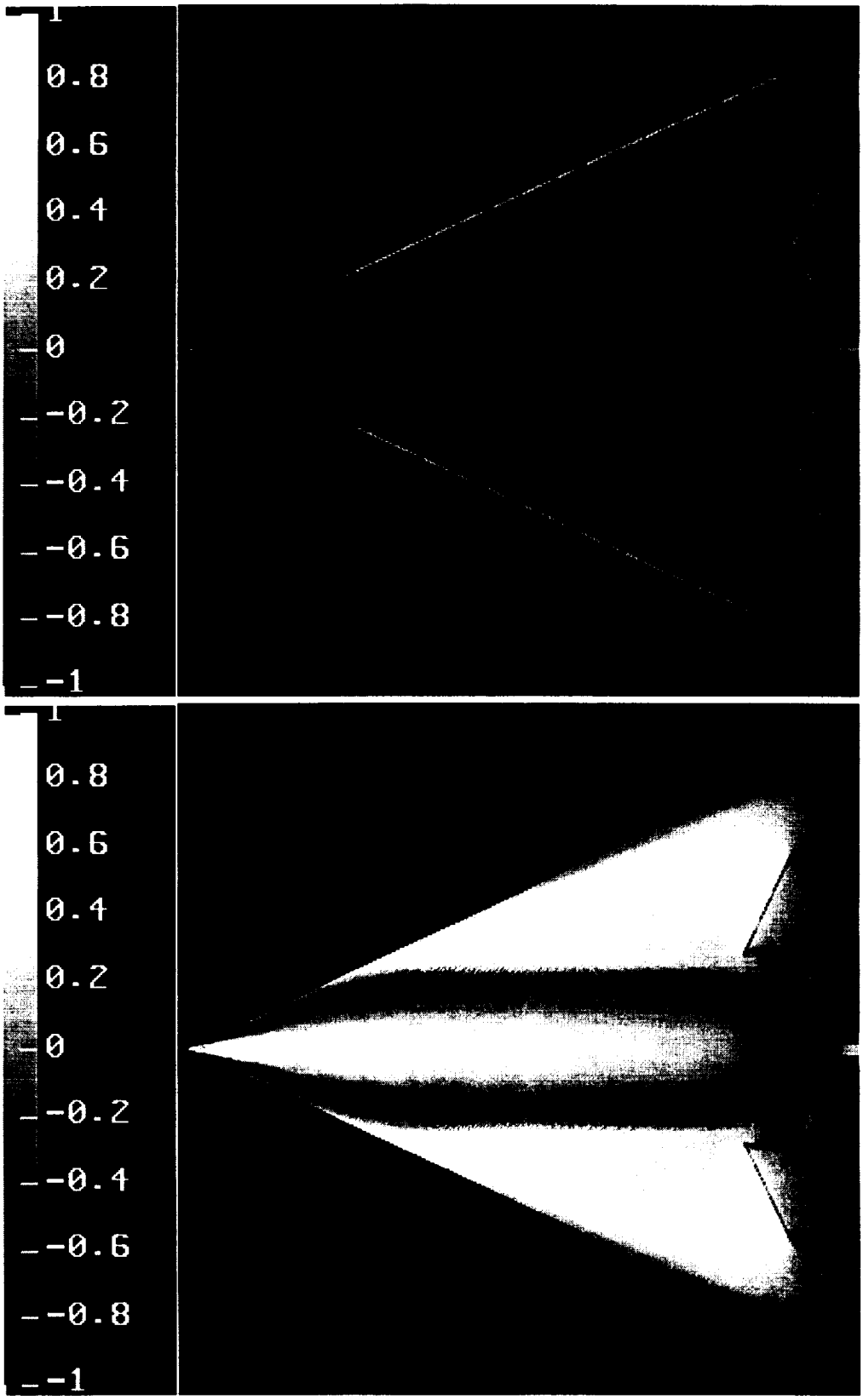

b. Deflected Elevon, M=0.9, α=20 deg

Figure 13. Continued

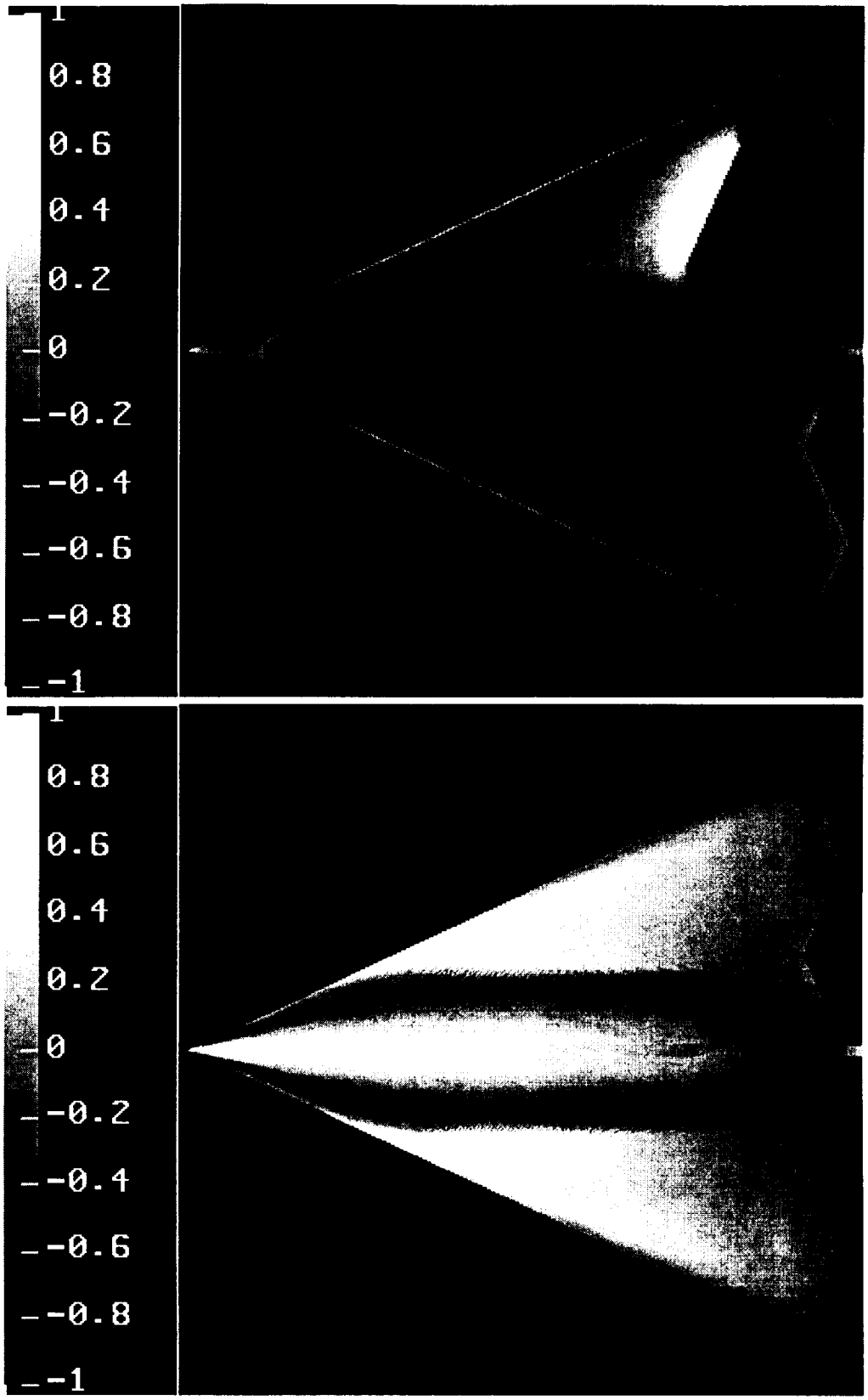

c. Deflected Spoiler, M=0.9, α=10 deg

Figure 13. Continued

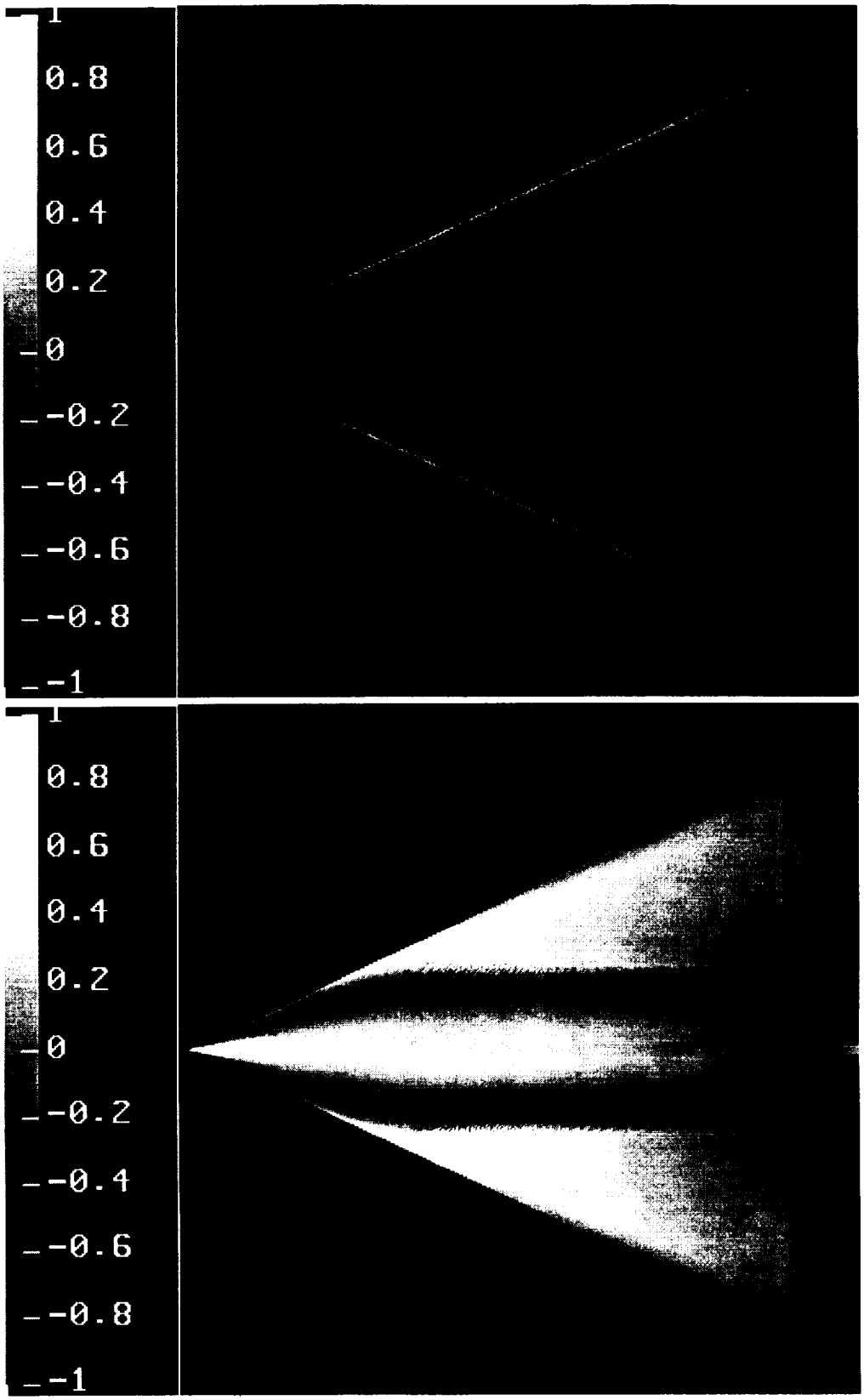

d. Deflected Spoiler, M=0.9, α=20 deg

Figure 13. Concluded

a. Deflected Elevon, M=0.9, α=10 deg

b. Deflected Elevon, M=0.9, α=20 deg

Figure 14. Particle Traces for Deflected Control Cases, M = 0.9

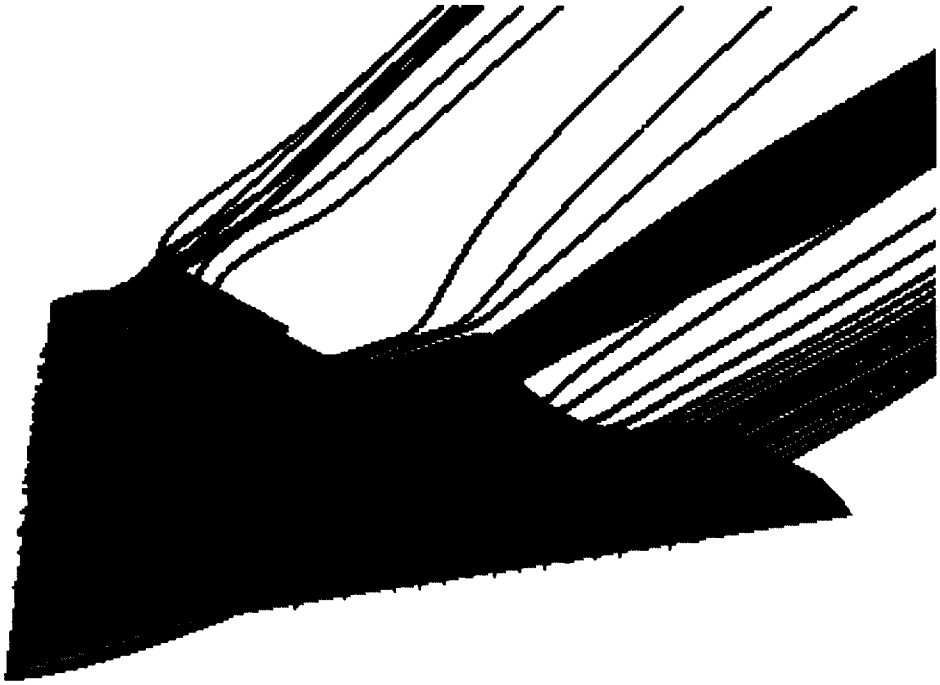

c. Deflected Spoiler, M=0.9, α=10 deg

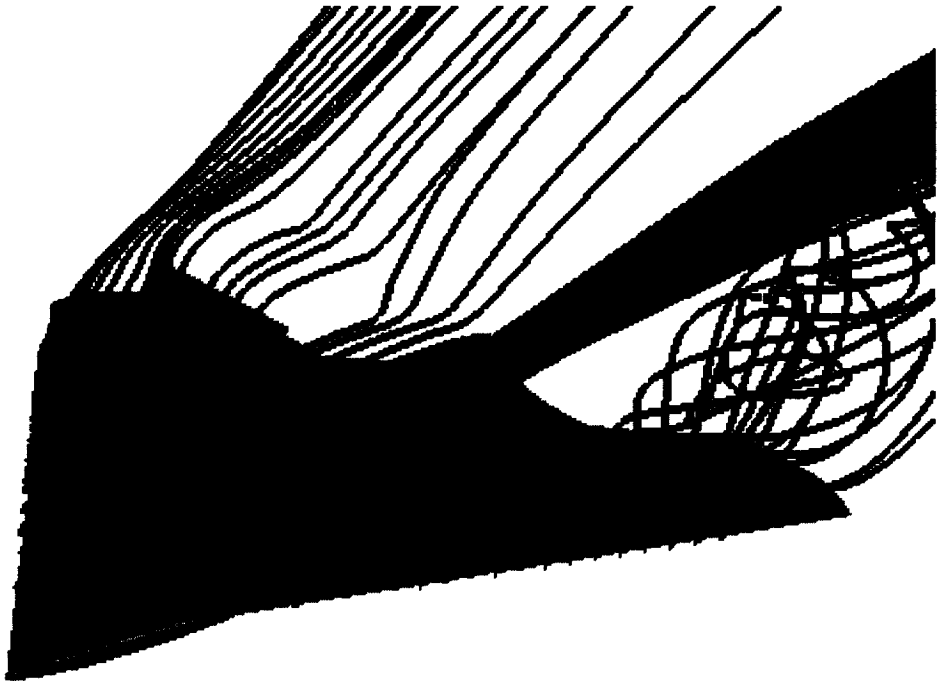

d. Deflected Spoiler, M=0.9, α=20 deg

Figure 14. Concluded

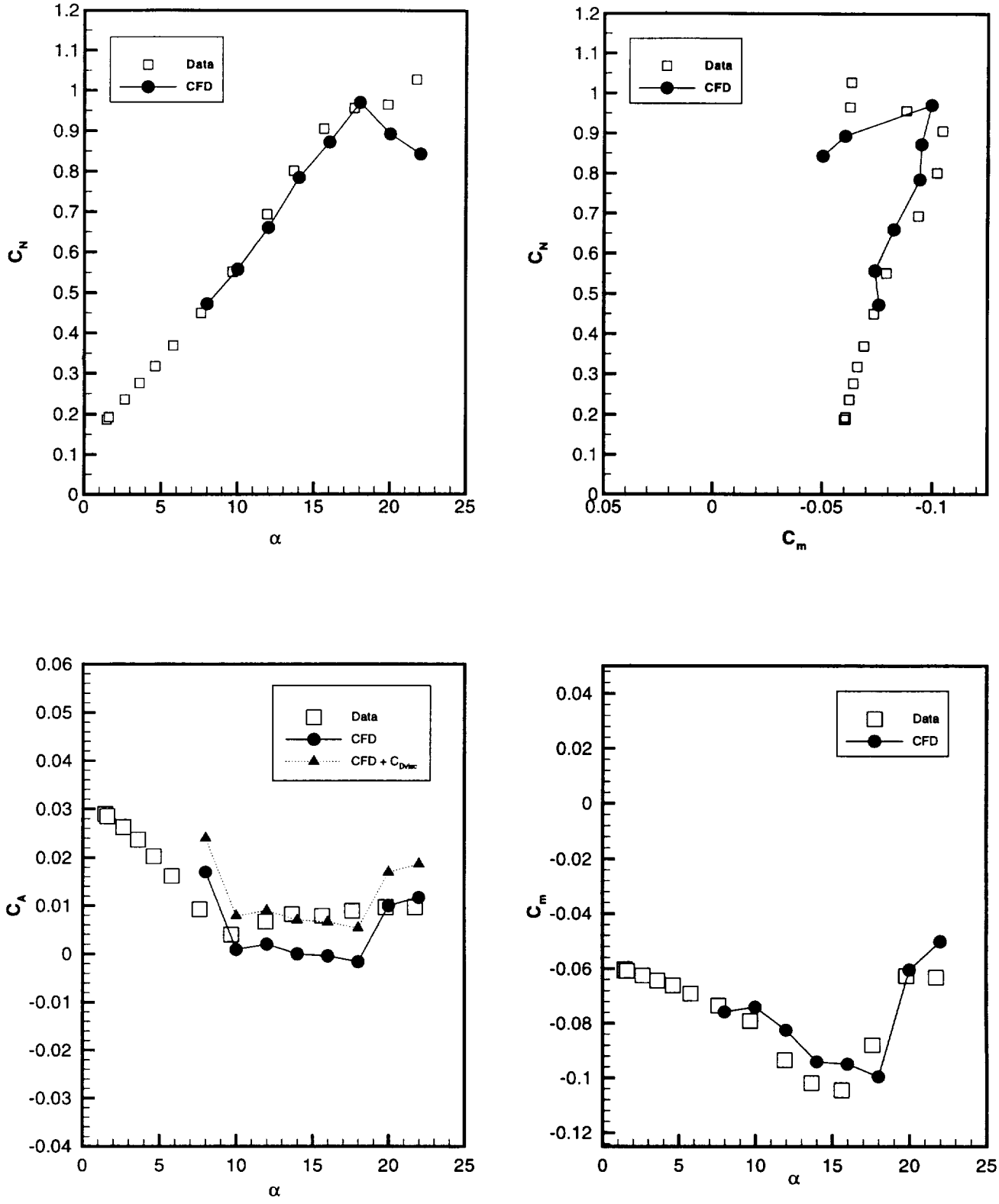

a. Deflected Elevons, M=0.9

Figure 15. Integrated Load Comparisons for Deflected Control Cases, M = 0.9

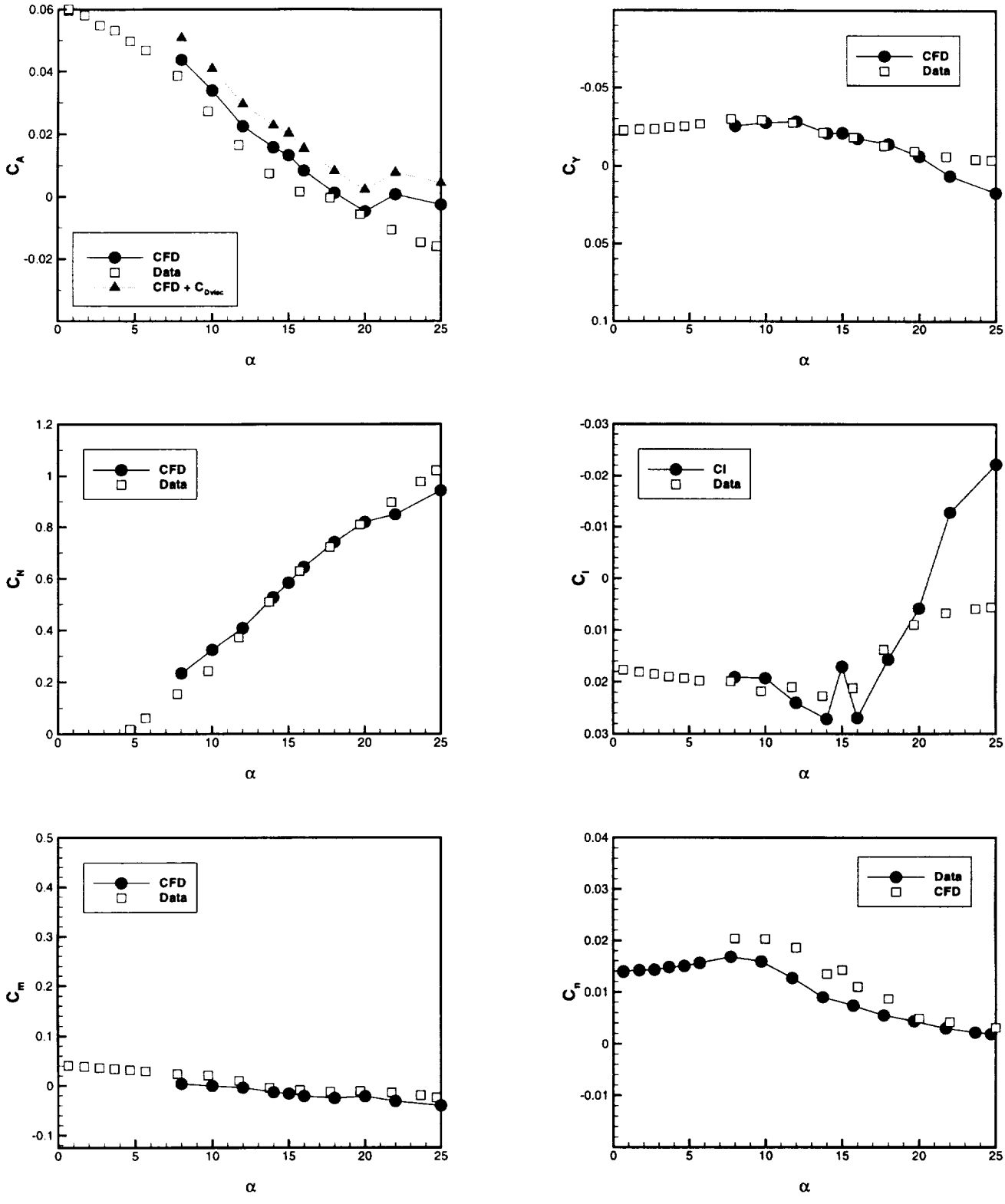

b. Deflected Spoiler

Figure 15. Concluded

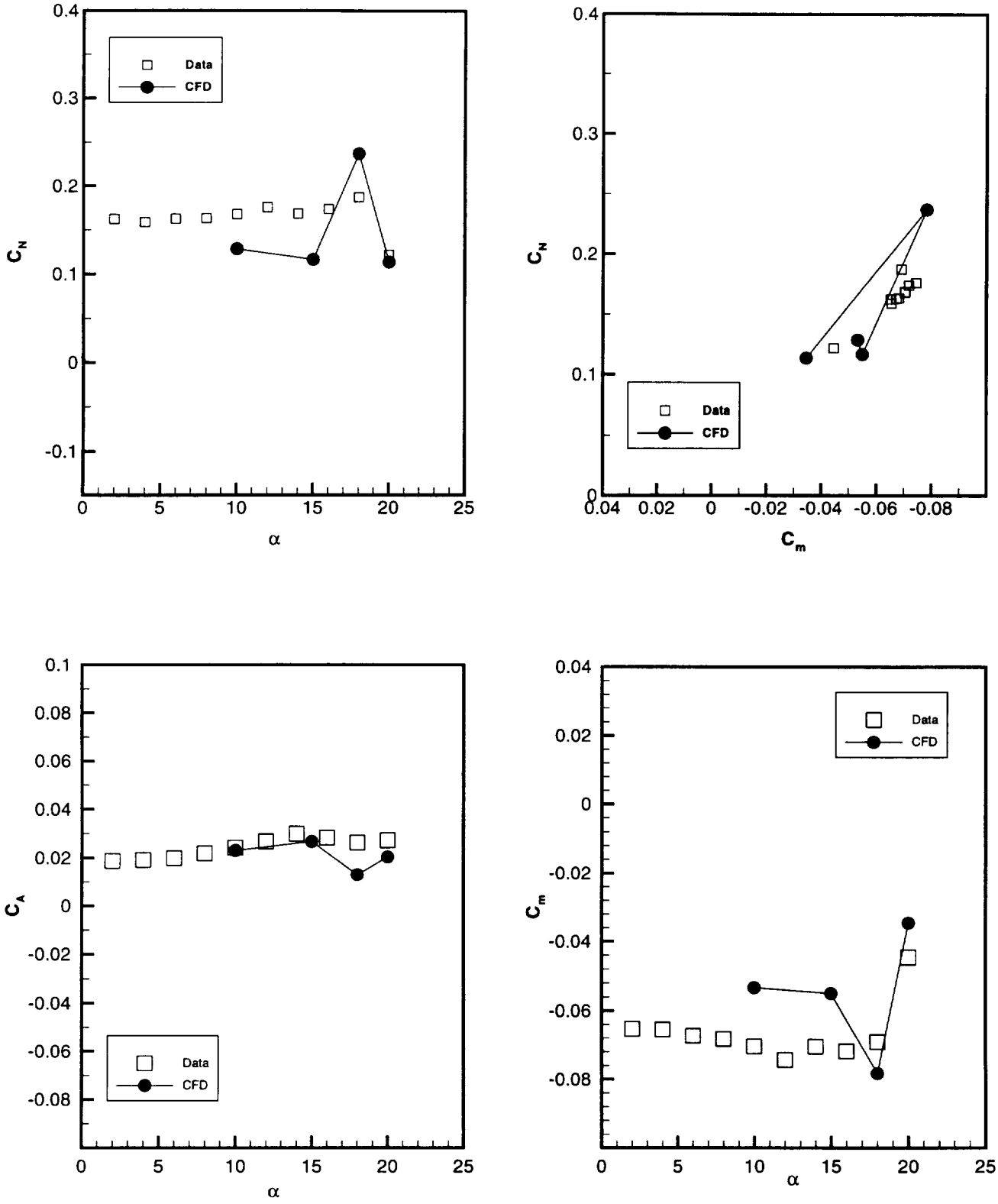

a. Deflected Elevon Increments

Figure 16. Increments of Integrated Loads for Deflected Control Cases, M = 0.9

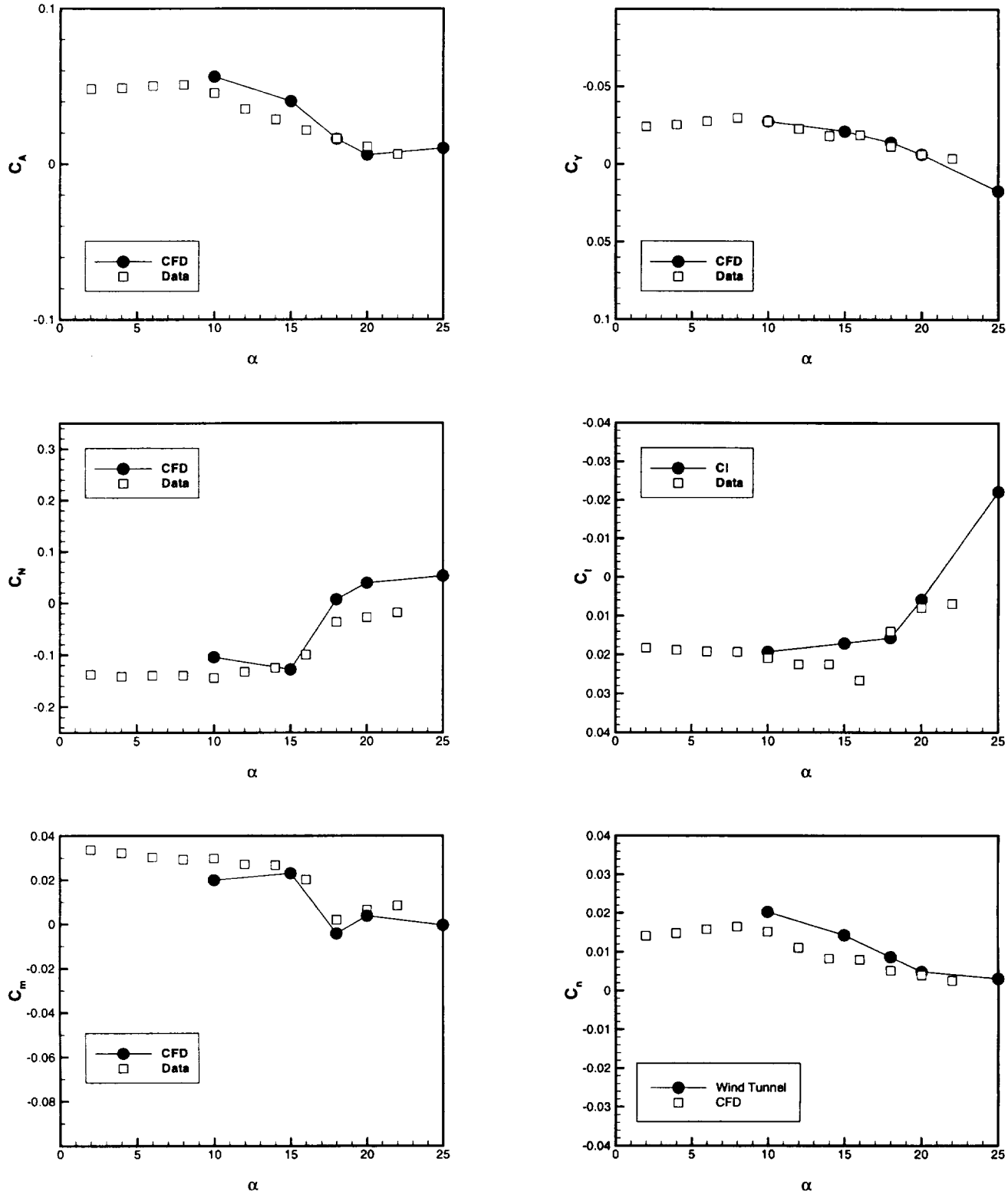

b. Deflected Spoiler Increments

Figure 16. Concluded

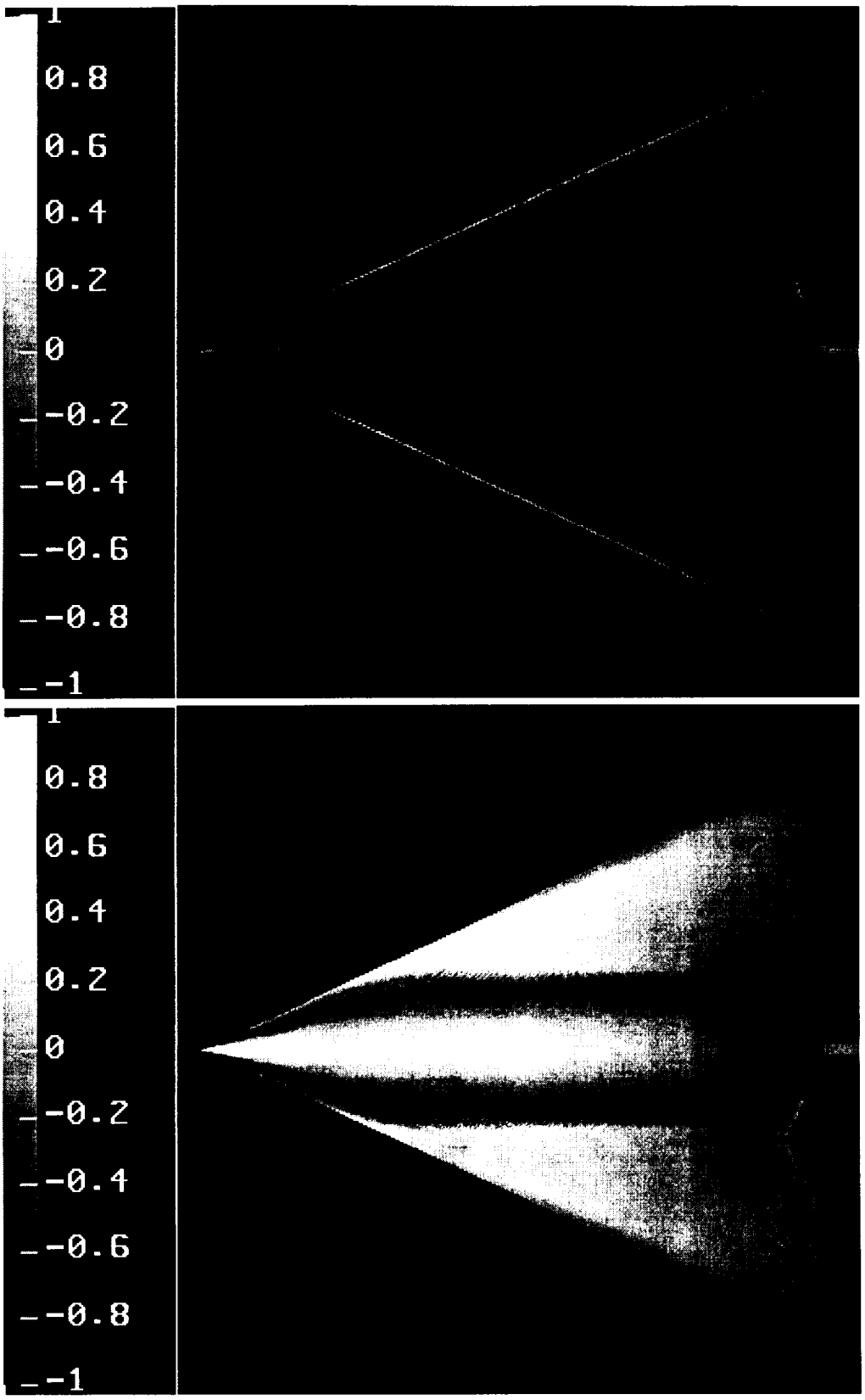

a. Baseline, M=0.9, α=20 deg, β = 4 deg

Figure 17. Surface C_p Contours for Baseline at β Cases, M = 0.9, α = 20 deg.

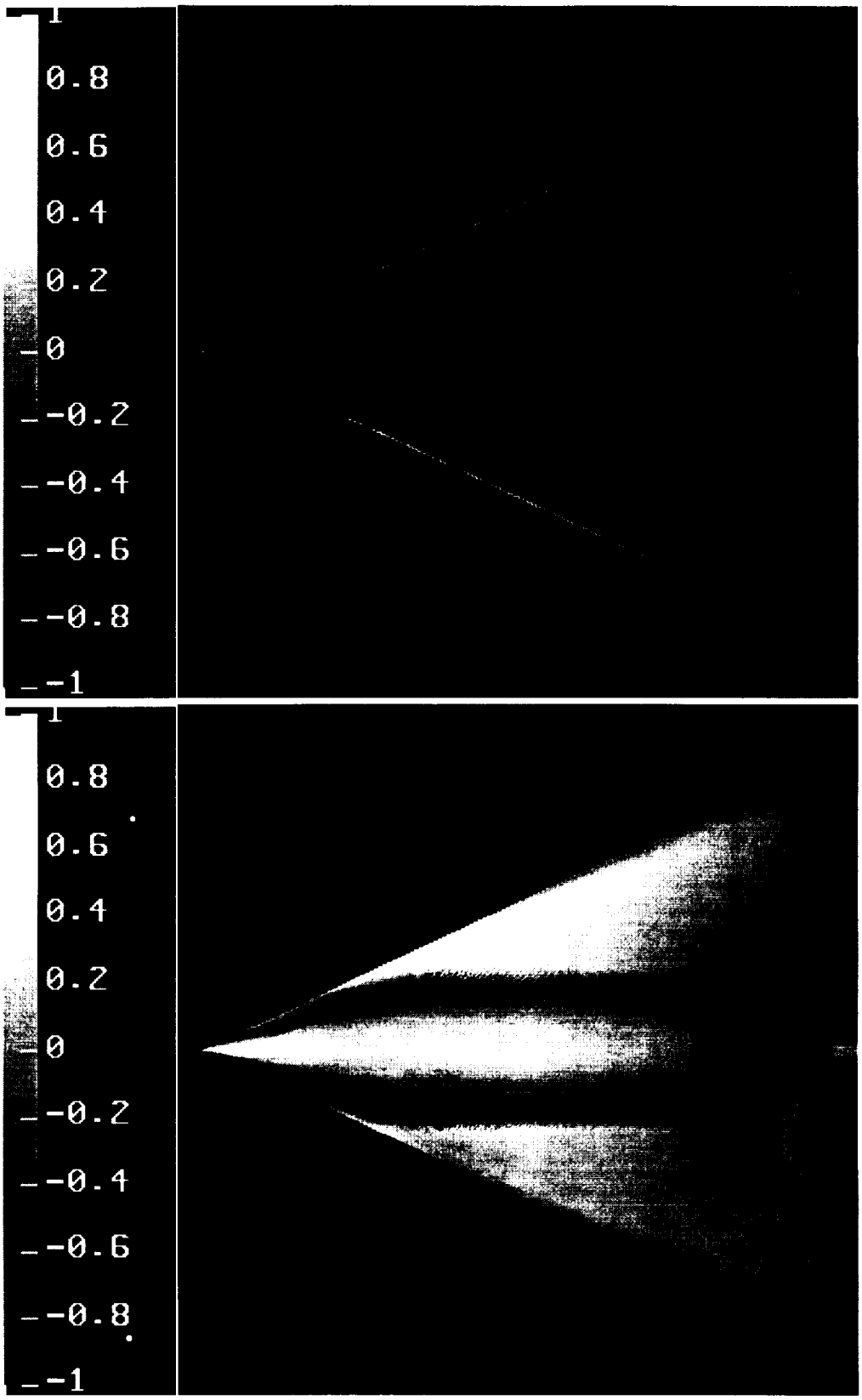

b. Baseline, M=0.9, α=20 deg, β = 8 deg

Figure 17. Concluded

a. M=0.9, α = 20 deg, β = 4 deg.

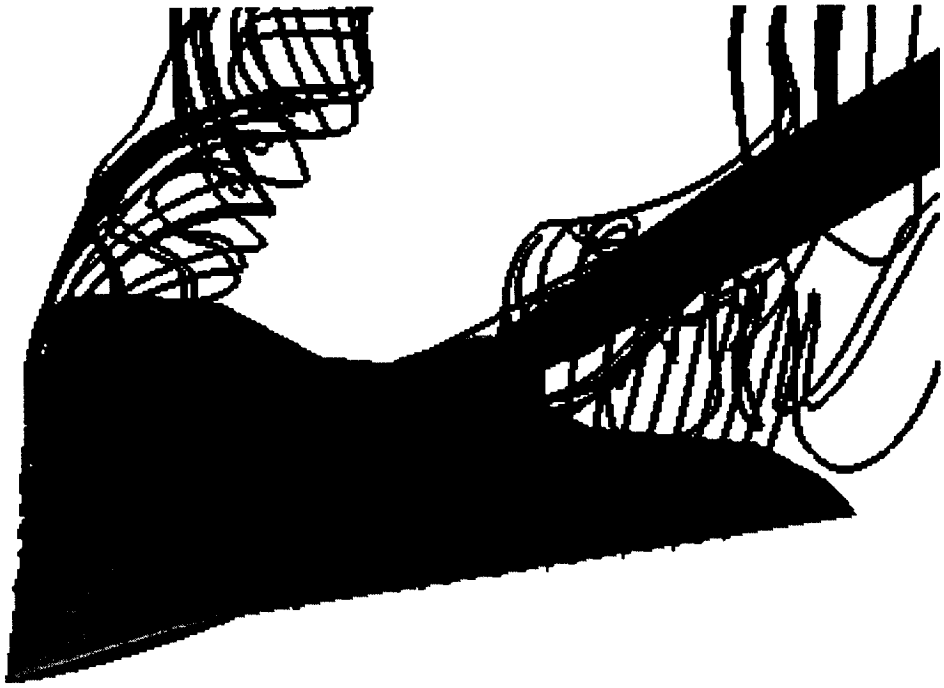

b. M=0.9, α = 20 deg, β = 8 deg.

Figure 18. Particle Traces for Baseline at β Cases, M = 0.9, α = 20 deg.

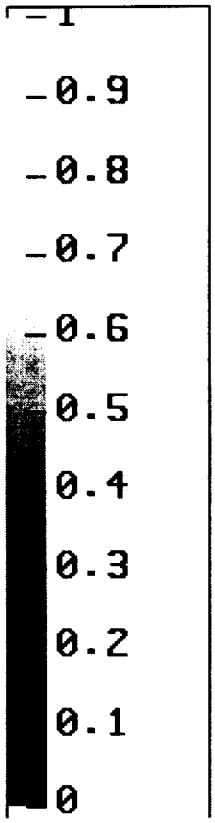

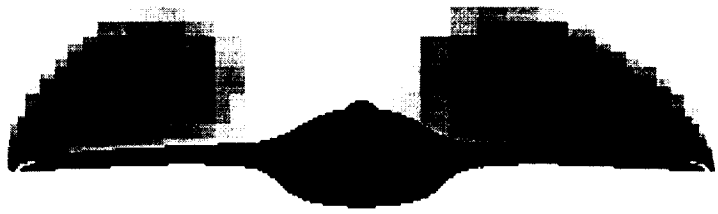

a. M=0.9, α = 20 deg, β = 4 deg.

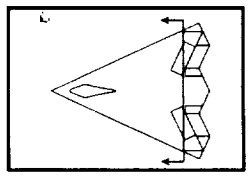

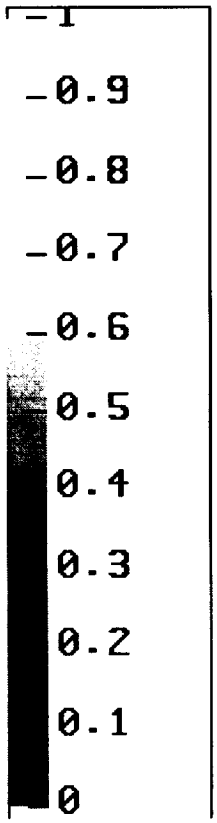

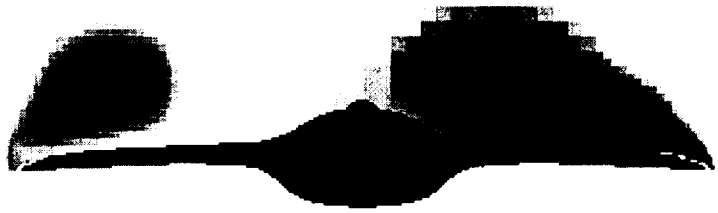

b. M=0.9, α = 20 deg, β = 8 deg.

Figure 19. Normalized Stagnation Pressure for Baseline at β Cases, M = 0.9, α = 20 deg

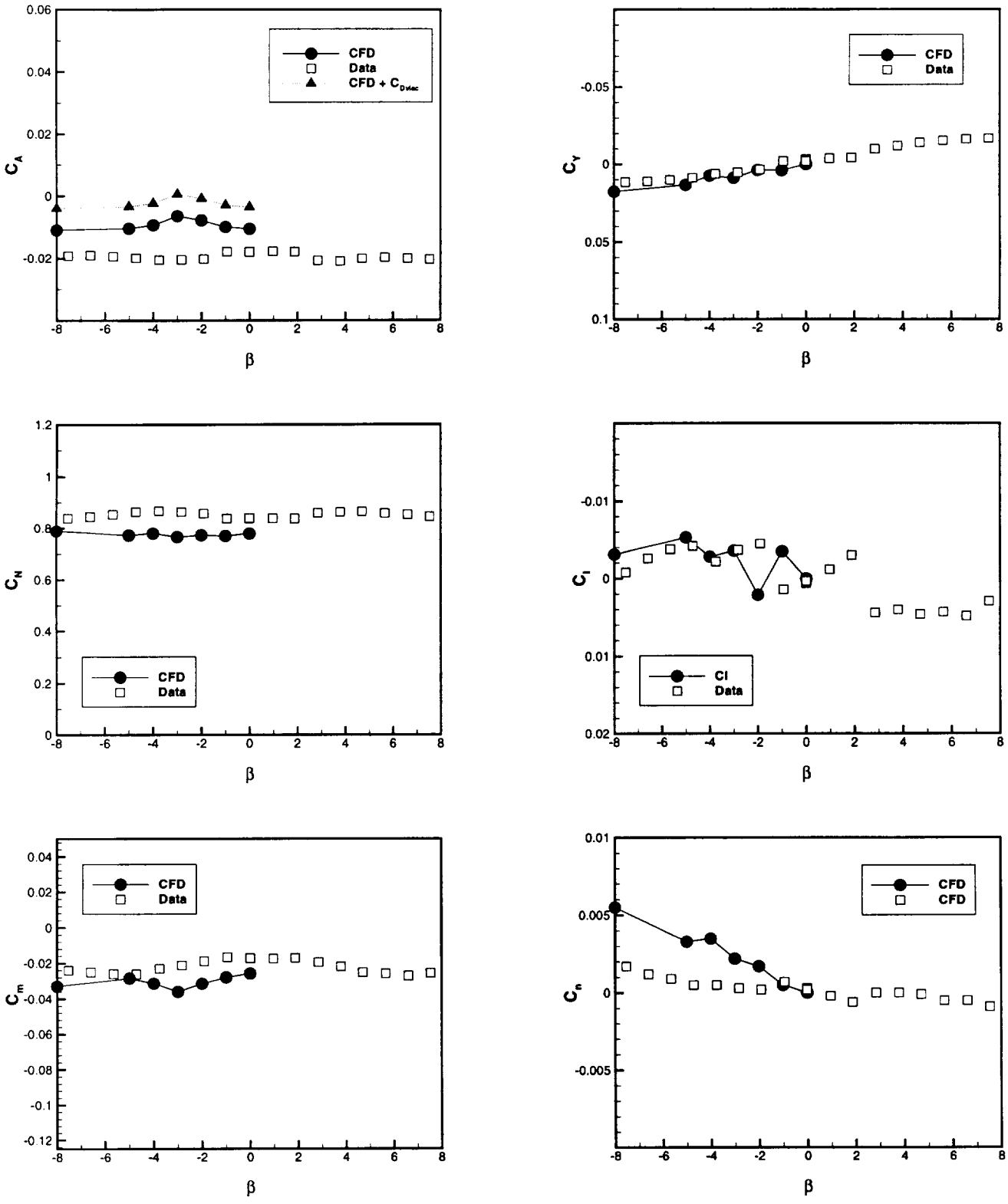

Figure 20. Integrated Load comparisons for Baseline at β Cases, M=0.90, α = 20 deg

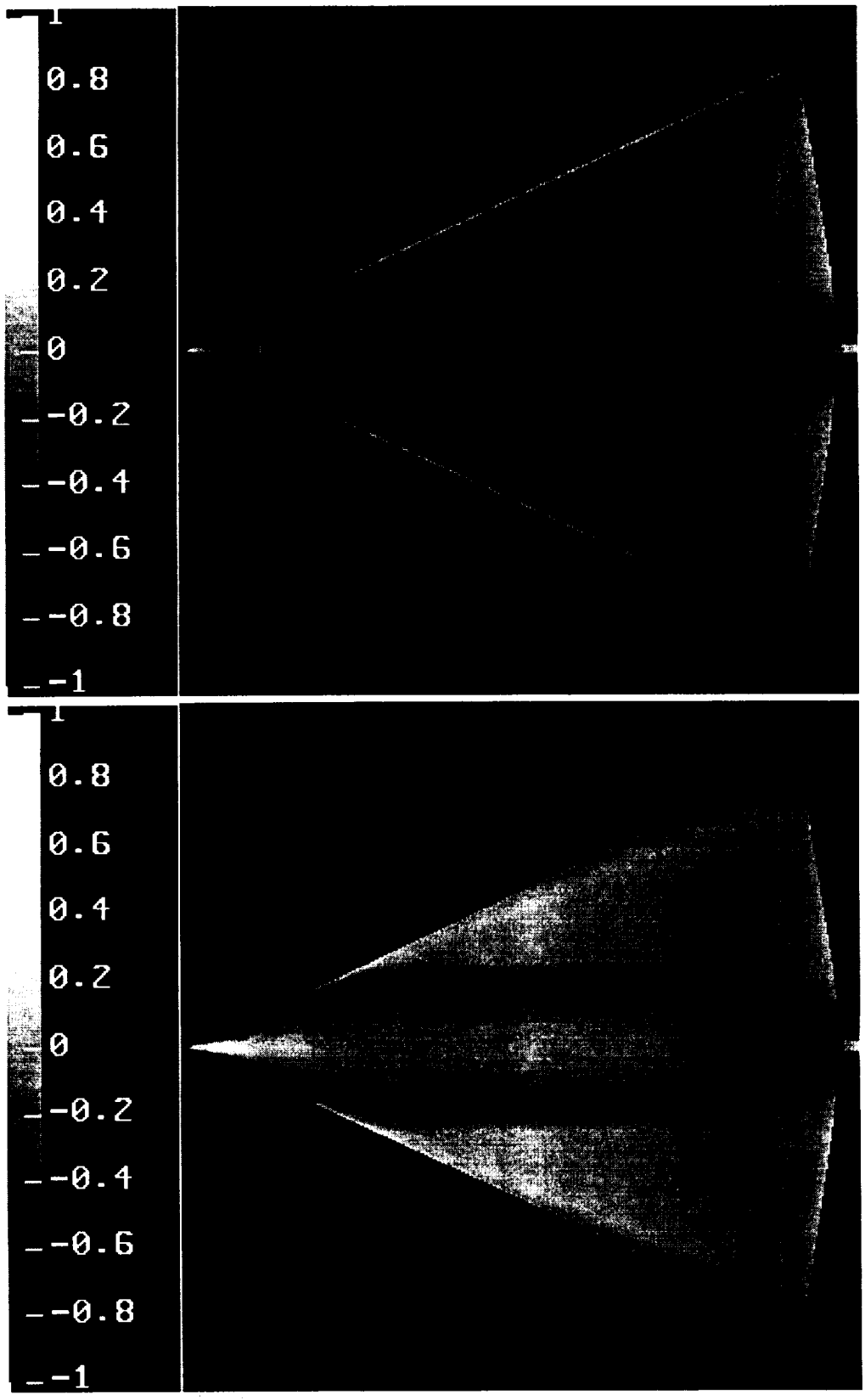

a. Straight Trailing Edge, M=0.9, α=10 deg

Figure 21. Surface C_p Contours for Straight Trailing Edge Cases, M = 0.9

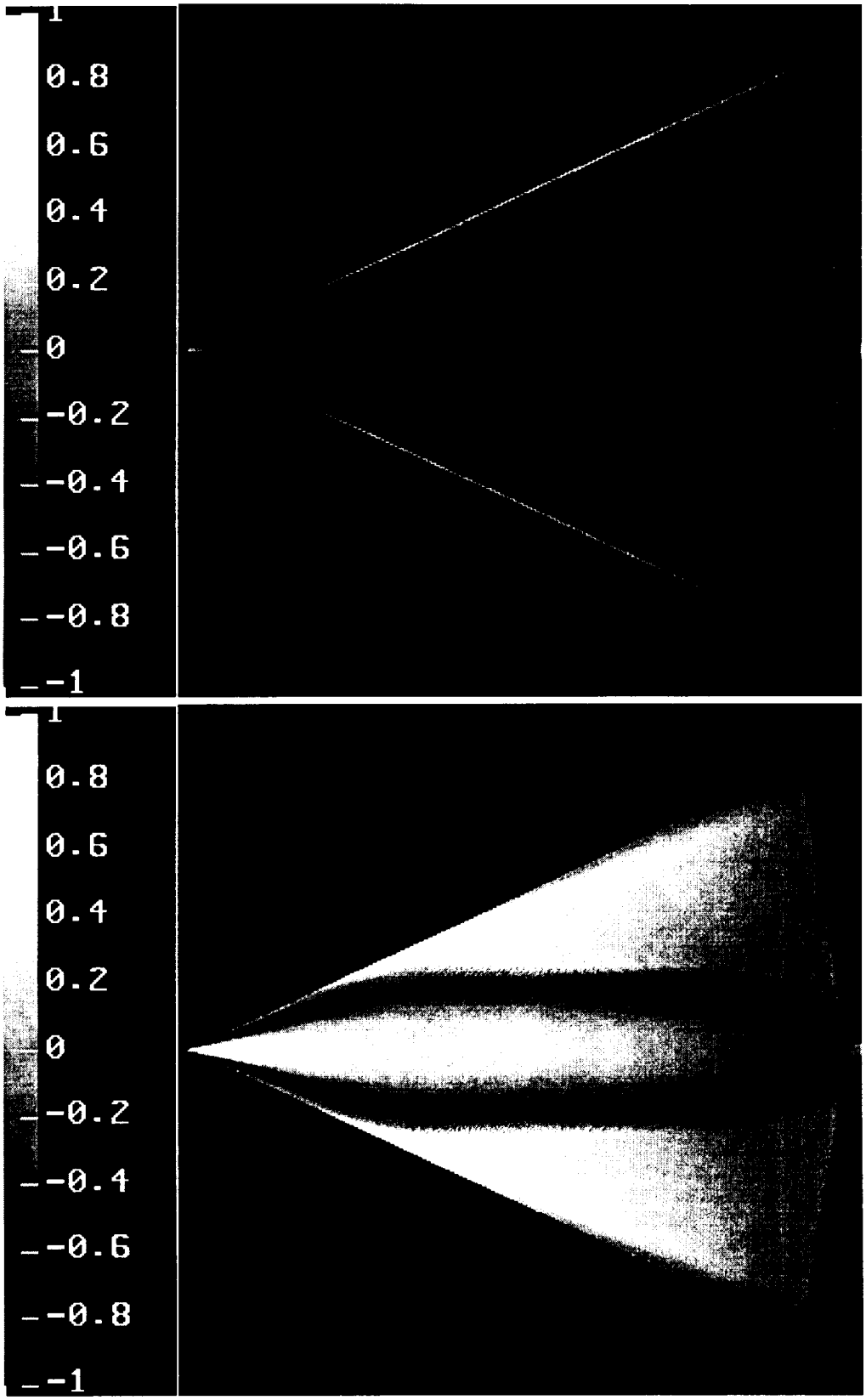

b. Straight Trailing Edge, M=0.9, α=20 deg

Figure 21. Concluded

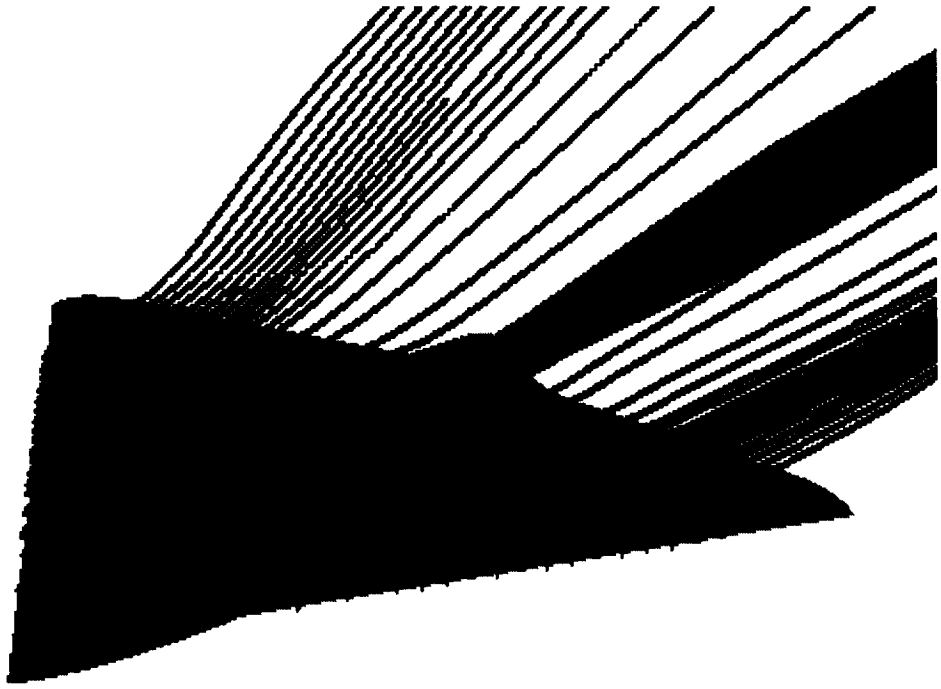

a. Straight Trailing Edge Configuration, M=0.9, α = 10 deg.

b. Straight Trailing Edge Configuration, M=0.9, α = 20 deg.

Figure 22. Particle Traces for Straight Trailing Edge Cases, M = 0.9

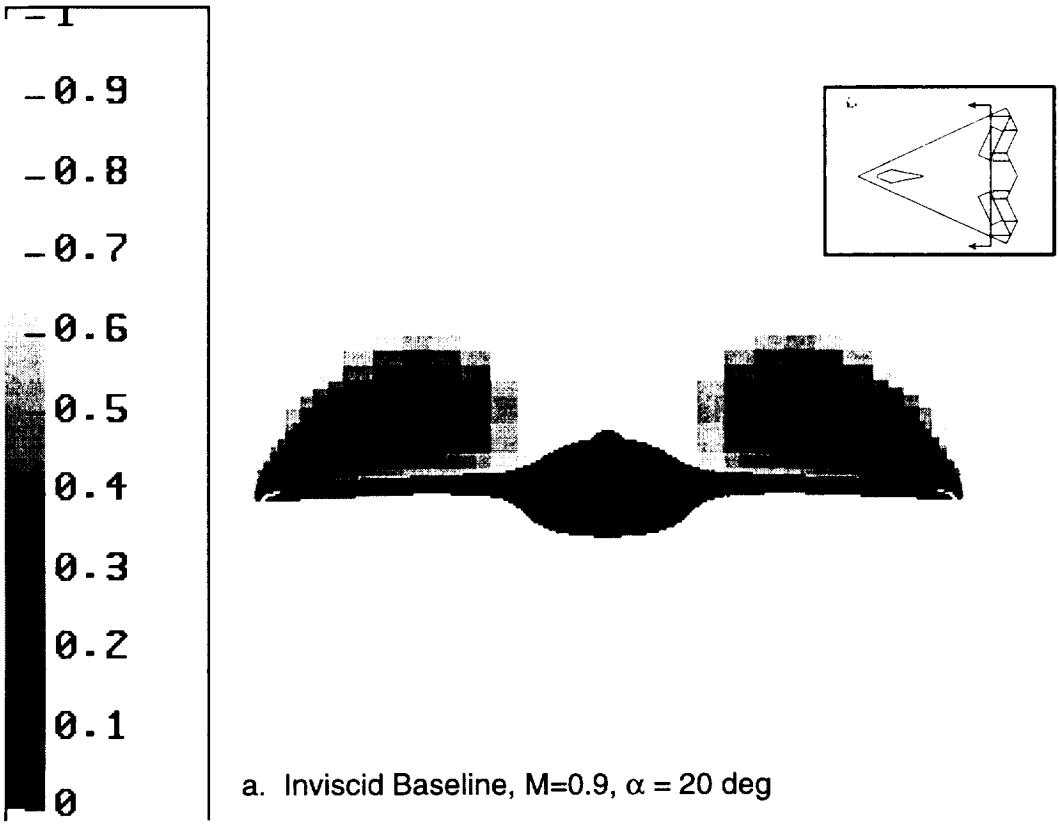

a. Inviscid Baseline, M=0.9, α = 20 deg

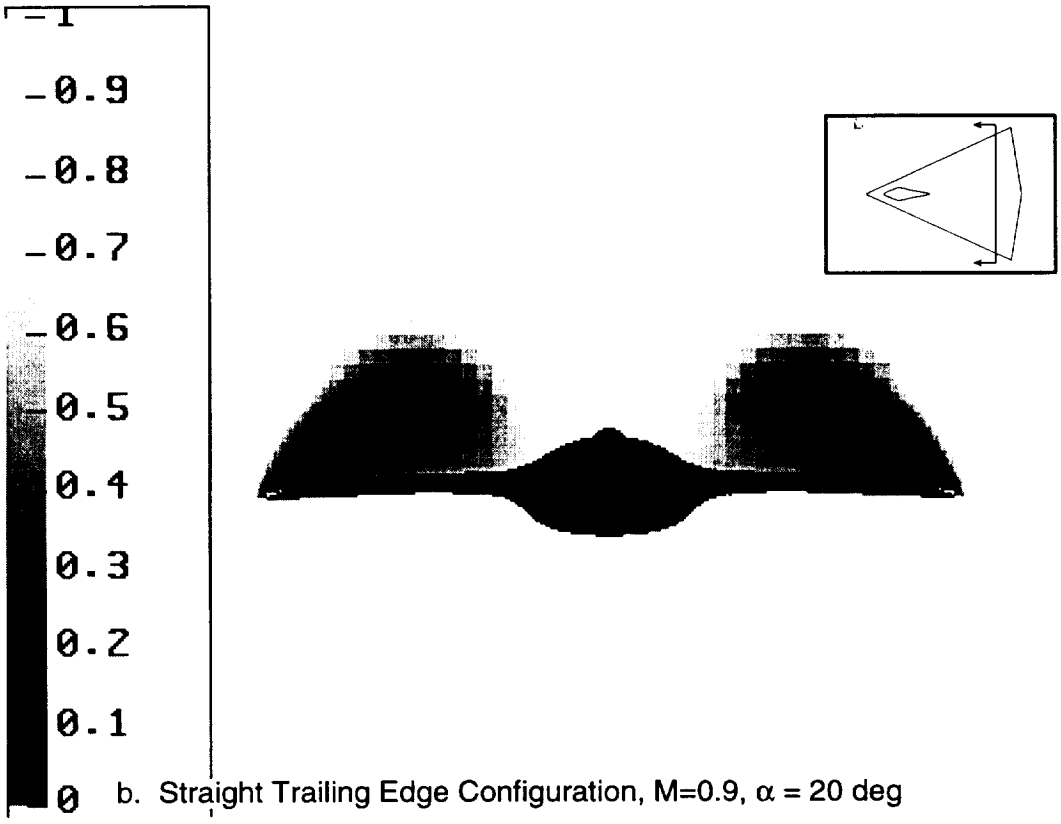

b. Straight Trailing Edge Configuration, M=0.9, α = 20 deg

Figure 23. Normalized Stagnation Pressure Contours for Straight Traling Edge Cases, M = 0.9, X=2.0 ft.

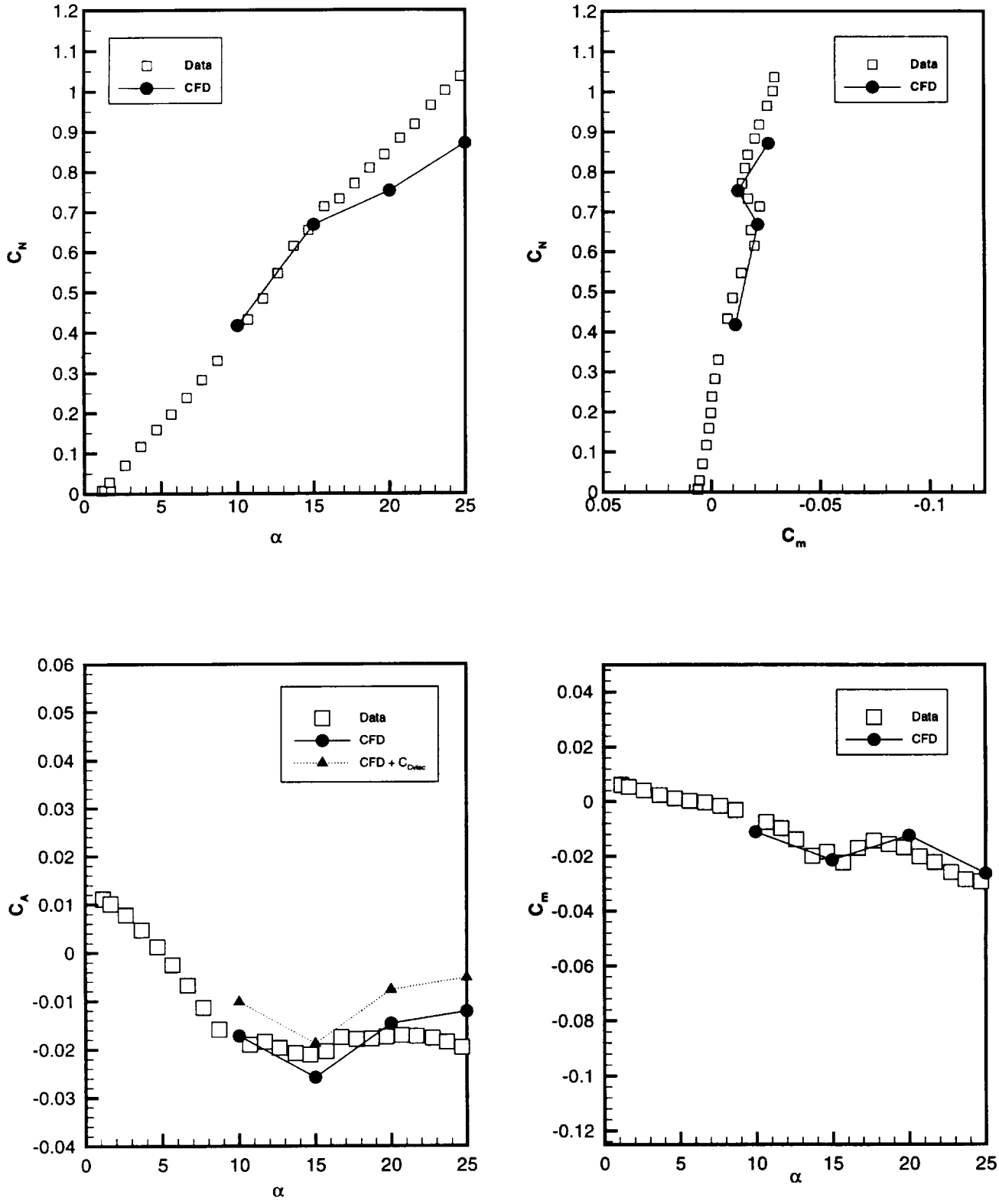

Figure 20. Integrated Load Comparisons for Straight Trailing Edge Cases, M=0.90